IMPROVING LOAD SHARING EFFICIENCY IN DRY FIBRILLAR ADHESIVES WITH INTERFACIAL CURVATURE AND THE ASYMPTOTIC SOLUTION TO OPTIMAL COMPLIANCE DISTRIBUTION

by

Harman Khungura

BASC, The University of British Columbia, 2018

A THESIS SUBMITTED IN PARTIAL FULFILLMENT OF THE REQUIREMENTS FOR THE DEGREE OF

MASTER OF APPLIED SCIENCE

in

The Faculty of Graduate and Postdoctoral Studies

(Mechanical Engineering)

THE UNIVERSITY OF BRITISH COLUMBIA

(Vancouver)

May 2021

The following individual certify that they have read, and recommend to the Faculty of Graduate and Postdoctoral Studies for acceptance, a thesis entitled:

Improving Load Sharing Efficiency in Dry Fibrillar Adhesives with Interfacial Curvature and the Asymptotic Solution to Optimal Compliance Distribution

Submitted by Harman Khungura in partial fulfillment of the requirements for

the degree of Master of Applied Science

in Mechanical Engineering

Examining Committee:

Mattia Bacca, Assistant Professor, Mechanical Engineering, UBC

Supervisor

Anasavarapu Srikantha Phani, Associate Professor, Mechanical Engineering, UBC

Supervisory Committee Member

Jamie Booth, Assistant Professor, Mechanical Engineering, California State University Northridge

Additional Examiner

Abstract

This thesis explores two investigations into improving the detachment strength and load distribution at the interface of dry bio-inspired fibrillar adhesives subjected to normal loading. The first is in how interfacial curvature affects the load sharing efficiency of engineering prototypes. Previous investigations unraveled the benefits of backing layer (BL) thickness in counteracting the detrimental load concentration created by interfacial misalignment. However, little attention was dedicated to the role of interfacial curvature on load distribution and the resulting adhesive strength. Based on the concavity of the curvature, the adhesive can detach more easily or develop stronger adhesion, compared to a flat-on-flat interface. This suggests the possibility to actuate curvature and better control adhesion. The curvature-induced strengthening/weakening of the adhesive was analyzed in combination to BL thickness, interfacial misalignment, and imperfections in the fibril length distribution. Detrimental load concentrations, created by BL interaction and interfacial misalignment, drastically reduce when the curvature prompts larger stretch to the central fibrils. This also mitigates load concentrations created by uneven fibril length distribution. These beneficial effects are reverted when the curvature prompts larger stretch to the peripheral fibrils. The quantitative analysis provides a design tool for stronger and more controllable adhesives.

The second investigation is into an asymptotic solution to the optimal compliance distribution attributable to fibrils within the array. The optimal compliance distribution allows the adhesive to achieve equal load sharing (ELS) which is its theoretical maximum strength i.e all fibrils carry the same load and detach simultaneously. The array of fibrils is modelled as a continuum of linear elastic material that cannot laterally transmit load (analogous to a Winkler soil). Ultimately, the closed form solution for the continuum distribution of fibril compliance is obtained and compared to the data from a discrete model. The results show improving accuracy for an incremental number of fibrils and smaller center to center spacing. Surprisingly, the approximation introduced by the asymptotic models shows reduced sensitivity of the adhesive strength with respect to misalignment and improved adhesive strength for large misalignment angles.

Lay Summary

Fibrillar adhesives are inspired by the reversible adhesive mechanisms found on small creatures such as the gecko. These creatures have shown the ability to attach and detach controllably to scale up vertical surfaces relying entirely on the hierarchical fibrillar structures on their toe pads. Synthetic mimics of these mechanisms are in the prototype stage and can benefit from the incorporation of beneficial or optimized geometric design principles. This work studies demonstrates how introducing a curvature throughout the array and tailoring each fibril to a calculated value will improve the strength and controllability of adhesion.

Preface

This dissertation is original and an independent work by the author, Harman Khungura. The main ideas in this research are his own, but the progress of this project would not be possible without Dr. Mattia Bacca's supervision. Dr. Bacca suggested the underlying mathematical model for the work but Harman Khungura developed the simulations and finite element analysis models within the commercial software MATLAB and ABAQUS himself.

A version of Chapter 2 and 3 has been published. Harman Khungura, Mattia Bacca (2020) Optimal Load Sharing in Bioinspired Fibrillar Adhesives: Asymptotic Solution. Journal of Applied Mechanics. 88(3). Harman Khungura conducted all analysis and wrote a portion of the manuscript. Mattia Bacca revised the manuscript and provided input on illustrations. Another version of Chapter 2 and 3 has been accepted by the Journal of Mechanics of Materials. Harman Khungura, Mattia Bacca (2021) The Role of Interfacial Curvature in the Detachment Strength of Bioinspired Fibrillar Adhesives. Journal of Mechanics of Materials. Harman Khungura conducted all analysis and wrote a portion of the manuscript. Mattia Bacca revised the manuscript and provided input on illustrations.

Contents

List of Figures

Acknowledgements

I extend my gratitude and appreciation to my supervisor Dr. Mattia Bacca for his expert guidance, but most importantly his welcoming nature which allowed me to feel at ease during my research.

Thank you to my lab colleagues Stefano Fregonese and Farid Hoseynian for your input during seminar rehearsals and presentations as well as suggestion on finite element modelling.

My appreciation to the faculty, and department staff for providing me with the facilities, resources and safe work environment to complete my research.

Dedication

Dedicated to my fiancée Anu Gill for her continuous love and encouragement.

1 Introduction

1.1 Applications for Reversible Adhesives

Reversible adhesion has significant applications in growing fields of research and exploration. Climbing robots can greatly benefit in their efforts in extraterrestrial and terrestrial exploration. The handling and insertion of gaskets in microfluidics could be greatly facilitated with reversible adhesives allowing for simple attachment and removal. There is also applications in mechanical grippers or pick and place handlers as there is a need to handle objects non-destructively without relying on vaccuum or cappillary forces. These applications are compatible with two modes of detaching a reversible adhesives, through either shear or orthogonal detachment. This work focuses on applications of orthogonal adhesives.

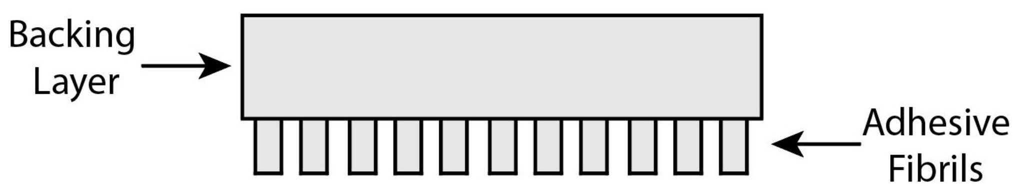

Figure 1: Generalized depiction of a dry fibrillar reversible adhesive.

1.2 Inspiration for Fibrillar Adhesives

Researchers have looked to nature for inspiration to develop dry reversible adhesive mechanisms. Many species of insects and small creatures such as the gecko possess reversibly adhesive mechanisms at their toe pads that allow them to scale vertical surfaces[1–4]. Geckos are of particular interest due to their relatively large mass. Research into the gecko's toe pads reveals hierarchical structures that consist of lamellae, setae and spatulae [5]. The end structures of this hierarchy are the spatulae, which are sub-micrometer in diameter while several micrometers in length scale. The predominant contributor to the adhesive ability of these structures are the van der waals interactions that occur between the fibril tips and the substrate [6, 7]. Van der waals interactions are weak short ranged interactions which suggests that mechanics play a role in determining the strength of these adhesives.

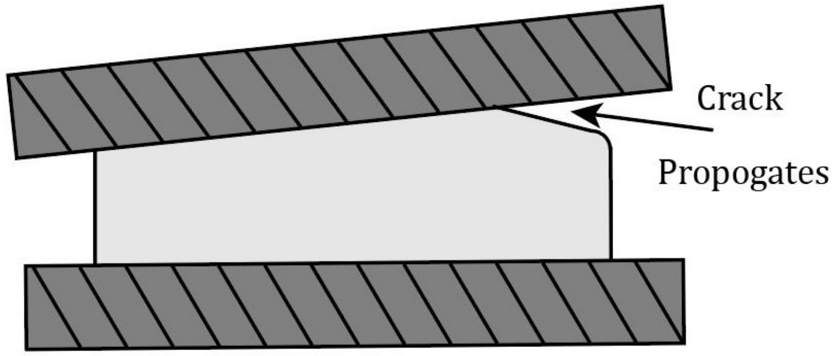

(a) A continuum adhesive interface

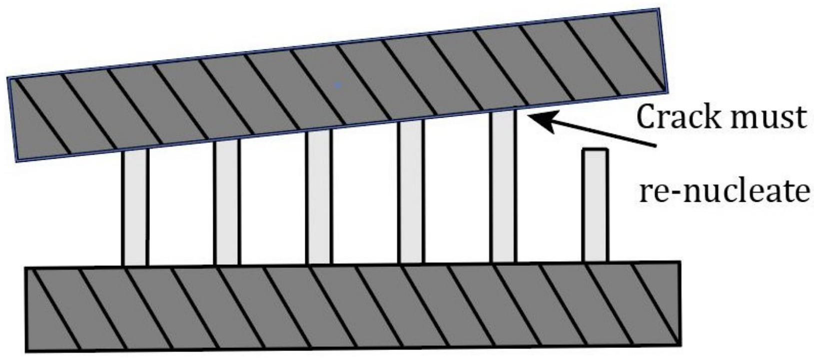

(b) A sub-divided adhesive interface

Figure 2: Showcasing the crack propagation and re-nucleation in continuum and discrete adhesive interfaces.

1.3 Mechanics of Fibrillar Adhesion

Fibrillar adhesives are able to provide strong adhesive strength for a multitude of reasons. For instance, the discrete contact points of the fibrils themselves means that for detachment to propagate, it must be re-nucleated for every fibril [8]. The is analogous to the method of crack trapping, which is used to toughen a continuum [9]. The fibrils are also capable of conforming to surface roughness without accumulating significant amounts of strain energy in both natural systems and synthetic mimics [10–13].

There is also an inverse scaling effect that occurs. This results in the adhesive force increasing with a greater subdivision of terminal structures [14, 15]. Subdividing the contact area results in a larger surface area to volume ratio and less sensitivity to variations in tip geometry which leads to a more uniform stress distribution at the interface [15, 16]. In this case, detachment occurs due to cohesive stress rather than via propagation of an interfacial defects. Cohesive detachment emerges from the absence of load concentration, a condition called equal load sharing (ELS) where local detachment of a fibril occurs only when the theoretical strength of adhesion is exceeded. This increases the strength of adhesion since variations in tip geometry and the induced stress concentrations are what cause failure to propagate and reduce overall strength [17, 18]. It should be noted that the absence of stress concentrations is only true below a critical size. The gecko's terminal adhering structures are at a nanometer-scale where as modern manufacturing capabilities cannot go below the micron-scale.

1.4 Established Design Principles

Manufacturing synthetic mimics at feasible length scales does not result in flaw insensitivity or conformation to finer surface asperities. This has led engineers to incorporate design strategies that mitigate load concentrations and strive towards ELS. Typically, the materials chosen to mold fibrillar dry adhesives are polydimethylsiloxanes (PDMS) and polyurethanes (PUs). These materials provide flexibility due to their low elastic moduli and can experience large strains at their break point. These culminate to provide good adhesive traits as the low stiffness leads to a slow build up of strain energy within the material.

Designs have begun to incorporate refined tip geometries as shown in Figure-??. Tip geometries that feature soft mushroom tips perform up to an order of magnitude greater than the conventional flat punch design due to their ability to mitigate edge stress concentrations and optimize adhesive strength [3, 19–21]. There has also been strategies that adopt stiffness grading along the longitudinal axis of the fibrils. This involves soft fibril tips while keeping stalks sufficiently rigid to avoid their mutual adhesion (fibril condensation). There is evidence to suggest that there are stiffness gradients throughout the setae of the adhesive pads of insects, which soft tips have the additional ability to better conform to surface roughness [22–24]. A similar approach has also been investigated for synthetic mimics to define new engineering design principles for these adhesives to enter a flaw-tolerant regime [25–27].

All of the above-mentioned investigations have been mainly focused on improving the design of the single adhesive unit and less attention has been dedicated to the design of these adhesives at the array scale. Engineers have incorporated a compliant backing layer (BL) into patterned microstructures which proves to be beneficial in the presence of misalignment at the interface and also helping micropillars conform to surface asperities [10–13, 24, 28]. The drawback of a

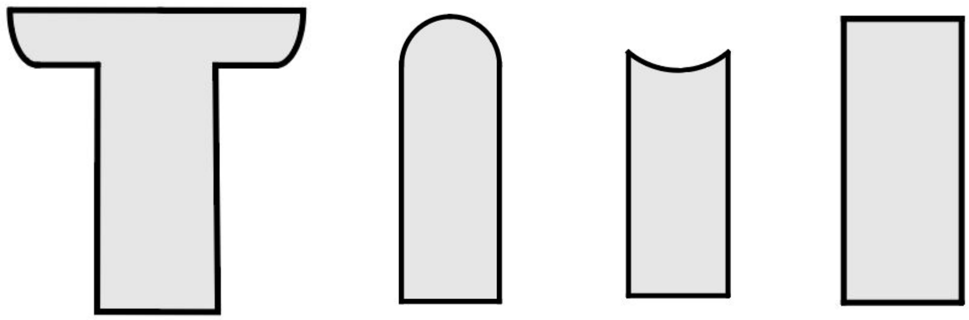

(a) Mushroom tip (b) Spherical tip (c) Concave tip (d) Flat tip

Figure 3: Showcasing common tip geometries implemented for fibrillar adhesive design.

circumferential load concentration at the edge of the array [29]. This reduces the strength or load sharing efficiency of the adhesive in the aligned case due to the mechanical coupling of backing layer interactions[24, 28]. The effects of BL compliance were calculated using contact mechanics solutions with the assumption that the BL is an infinite elastic half space. However, the effects are dependant on the thickness of the BL in proportion to a single fibril.

To counteract the non-uniformity in loading of fibrils incurred from the BL interactions, researchers have proposed the spatial tailoring of fibril stiffness [28, 30]. This results in ELS or the load being carried by each fibril being uniformly distributed throughout the array, hence leading to simultaneous detachment. Bacca *et. al* (2016) suggests a numerical model to determine the optimal compliance distribution of the fibrils within the array. This, however, comes with a computational cost and without the numerous benefits of an analytical solution. Of particular importance is the link between the physical properties of the adhesive and the contrast between the softest fibrils and the stiffest ones.

1.5 Objectives and Outline

Since engineered prototypes for reversible adhesives are incapable of operating within the flaw insensitive regime, a macroscopic model that provides quantitative design guidelines can aid the development of this technology. A currently unexplored strategy to reduce array-level load concentrations is the use of interfacial curvature. This work explores the effects of interfacial curvature in combination with interfacial misalignment, BL thickness and imperfections in fibril length distribution. Depending on the concavity of the curvature, the adhesive strength can be enhanced or drastically reduced. This provides the theoretical basis for the development of actuated interfacial curvature for enhanced adhesion control, i.e. strong adhesion and ease of detachment. A curvature incrementing the stretch of central fibrils produces an increment in adhesive strength, compared to a non-curved interface (flat-on-flat). This is because such an interfacial curvature counteracts BL interaction and the benefits are proportional to BL thickness. The incremented strength also produces a better resistance to interfacial misalignment and to imperfections on the fibril length distribution.

This work also proposes an asymptotic model, providing an analytical solution for the optimal compliance distribution for reversible adhesives in normal loading which overcomes the limitation of the numerical solution. The model represents the collection of fibrils as a continuum made of a linear elastic material that cannot laterally transmit load, analogous to a Winkler soil. The solution can be obtained in closed form for various shapes of the contact region between the adhesive and the adhered substrate. The solution is derived for the case of arrays with circular and square shapes since they provide symmetry and are relevant to engineering prototypes. However, the applicability of the method can extend to any array shape. The results obtained can be generalized to the case of an adhesive interface populated by brittle bonds of varying compliance. When the distribution of compliance matches the one proposed from the analytical model, the interface will reach maximum theoretical strength by minimization of stress concentration at its surface. This phenomenon has been experimentally observed in shear adhesion [31].

2 Design and Methods

2.1 Displacement Input Model and Analytical Solution for Rigid Backing Layer

This section covers the computational model that considers how BL thickness and curvature affect fibrillar detachment and the maximum detachment strength. First the model is constructed using contact mechanics solution for an infinite BL. Next the model is tailored for finite thickness BL that more accurately captures prototype geometry. The section concludes with the derivation of the analytical solution for the detachment strength of a rigid BL array with both interfacial curvature and misalignment.

2.1.1 Displacement Input Model for an Infinite Thickness Backing Layer

The computational model used in this work was run in MATLAB to calculate fibrillar detachment and load sharing efficiency and expands on the purely linear elastic models utilized in previous works [24, 28, 32, 33]. This model considers the adhesive as a homogeneous linear elastic material with Young's modulus E and Poisson's ratio ν that consists of an array of N cylindrical fibrils protruding from the surface of the BL as shown in Figure-4. The BL has a thickness H where as each fibril is of height h and stalk radius a. The fibrils in the array are packed with orthogonal distribution along the x and y-axes. Such a distribution is chosen due to mathematical simplicity, despite a hexagonal distribution along non-orthogonal axis providing more efficient packing. However, for the case of large and densely packed arrays, the influence of fibril packing on the final results is negligible.
The presence of interfacial misalignment and curvature are considered in the generalized displacement of the fibril tips. Interfacial misalignment in the x and y directions are defined by the misalignment ratios $\lambda_x = \tan\theta_{xz}$ and $\lambda_y = \tan\theta_{yz}$, respectively, with θ_{xz} and θ_{yz} being the misalignment angles. The interfacial curvatures in the x and y directions are identified as $\kappa_x = {}^1/_{R_x}$ and $\kappa_y = {}^1/_{R_y}$ where R_x and R_y are the radii of curvature. The displacement at the tip of fibril i then becomes

$$u_i = \overline{u} + \lambda_x x_i + \lambda_y y_i + \frac{\kappa_x x_i^2}{2} + \frac{\kappa_y y_i^2}{2} \tag{1}$$

where x_i & y_i are the coordinates of the centre of fibril i with respect to the coordinate system shown in Figure-4 and $\overline{u}$ represents the displacement of the rigid substrate (RS). For the purpose of this study, the interfibrillar spacing is constant throughout the array and denoted as d.

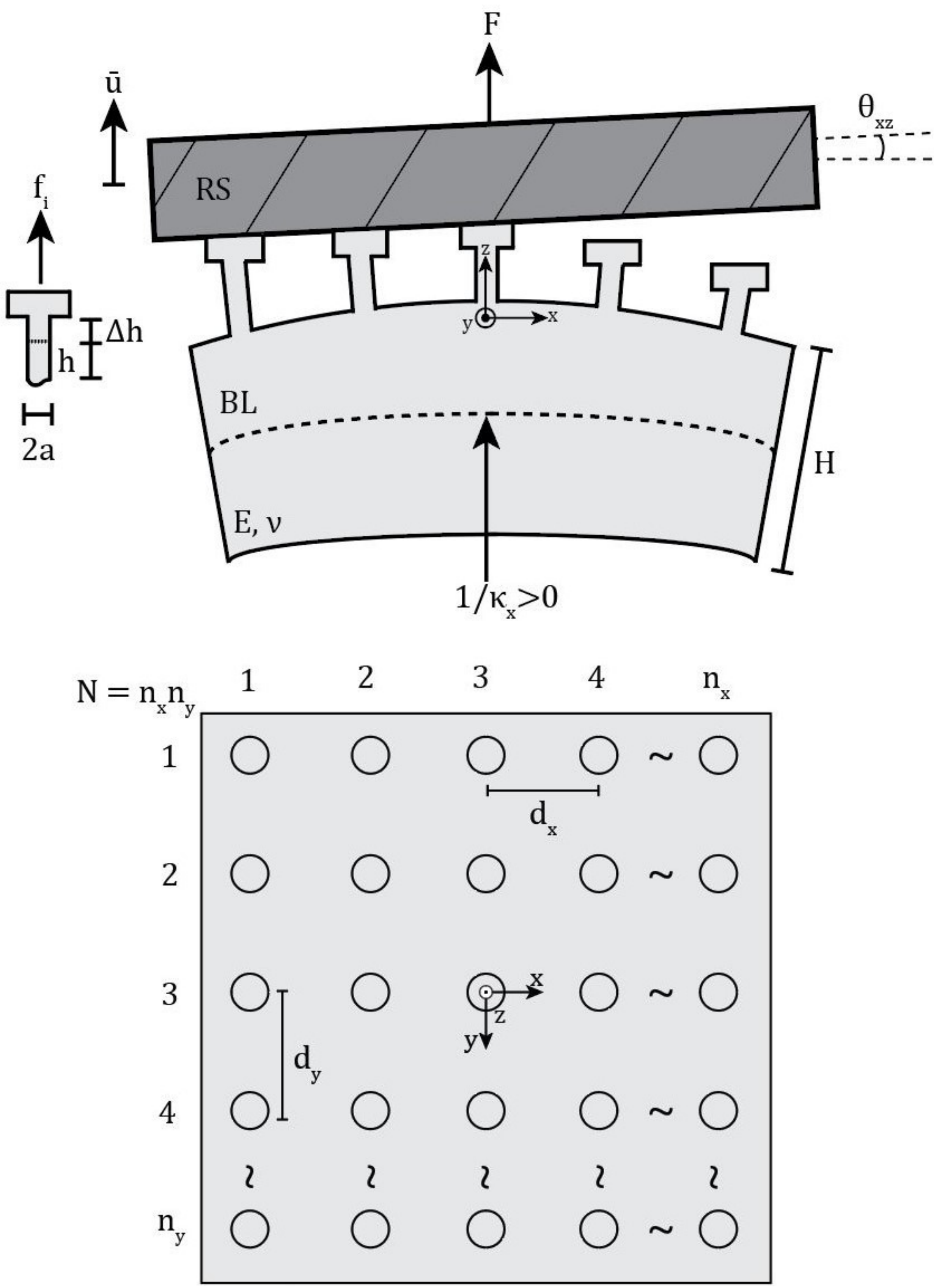

Figure 4: Schematic of the model simulating the detachment of the fibrillar adhesive

By performing a force balance on the adhesive system in Figure-4, it becomes apparent that the total force must be equal to the sum of the axial forces of all attached fibrils within the array.

$$F = \sum_{i=1}^{N} f_i \tag{2}$$

The above expression can be normalized to represent what percentage of the maximum theoretical adhesive strength is being exerted on the array. This is done as:

$$\tilde{F}_{max} = \frac{F}{N f_{max}} \tag{3}$$

where f_{max} is the maximum local strength of adhesion of a single fibrillar unit. The value of $\tilde{F}_{max}$ is also an indication of how well the adhesive strength of a single fibril scales throughout the array. As for contact between the fibril tip and the RS, it is assumed that perfect contact and adhesion occurs.

The total displacement of a fibril tip u_i is also expressible as the combination of the axial strain experienced by fibril i and the BL deformation beneath it. This can be expressed as a superposition of the two deformations and is given in the equation:

$$u_i = u_i^{fib}(f_i) + \sum_{j=1}^{N} u_i^{BL}(f_j) \tag{4}$$

where $u_i^{fib}(f_i)$ is simply the elongation due to axial strain within the fibril given by Equation-5. The second term, $\sum_{j=1}^{N} u_i^{BL}(f_j)$ is the total BL deformation directly below fibril i due to the pulling force exerted onto the BL by all active fibrils in the array $(j \in \mathbb{Z} \cap [1, N])$.

$$u_i^{fib}(f_i) = \frac{h f_i}{\pi a^2 E} \tag{5}$$

The BL deformation underneath fibril i due to force f_i was taken to be the average value of the contact mechanics solution for the surface displacements on an infinite elastic half space caused by a uniform stress applied over a contact radius a [34]. This computes to the expression given in Equation-6 below where $E^* = {}^{E}/_{1-\nu^2}$.

$$u_i^{BL}(f_i) = \frac{16 f_i}{3\pi^2 a E^*} \tag{6}$$

The pulling force f_j that causes BL deformation underneath fibril i for $i \neq j$ can be approximated as a concentrated normal force acting on the surface of an elastic half space [28]. The contact mechanics solution for this provided by [34] is given in Equation-7 below where r_{ij} is the radial distance between fibrils i & j. The superposition of displacement profiles from a concentrated force and Euler-Bernoulli beam in bending are validated in Appendix B.

$$u_i^{BL}(f_j) = \frac{f_j}{\pi E^* r_{ij}} \quad \text{for } j \neq i \tag{7}$$

The total displacement of the fibril tip given in Equation-4 can be expressed as a linear combination of Equation-5, Equation-6, Equation-7 and f_j. This results in the height of any fibril tip u_i being expressible as a product of a compliance matrix and a vector of the fibrillar forces acting throughout the array as shown in Equation-8.

$$u_i = C_{ij} \cdot f_j \tag{8}$$

The components of the compliance matrix are given in Equation-9a and Equation-9b.

$$C_{ij} = \frac{1}{\pi r_{ij} E^*}, \quad \text{for } j \neq i \tag{9a}$$

$$C_{ij} = \frac{1}{\pi a E^*}\left[\frac{16}{3\pi} + \frac{h}{a(1-\nu^2)}\right], \quad \text{for } j = i \tag{9b}$$

By inverting Equation-8, the force in any fibril j can be obtained from the stiffness matrix K_{ji} and the known displacement at the tip u_i.

$$f_j = K_{ji} \cdot u_i \tag{10}$$

2.1.2 Dimensional Analysis and Numerical Implementation of Model

All variables of length dimension are made relative to the radius of a fibril a except for the fibril tip displacement u_i. These variables are expressed below for reference.

$$\tilde{r} = \frac{r}{a}$$
$$\tilde{h} = \frac{h}{a}$$
$$\tilde{d} = \frac{d}{a}$$
$$\tilde{x} = \frac{x}{a}$$

The fibril tip displacement u_i is scaled by $u_n = \frac{\pi a E^*}{f_{max}}$ which is the nominal displacement. This scales the initial fibril tip displacements as shown in Equation-12 where $\tilde{\kappa}_x = {}^{\kappa_x a^2}/_{u_n}$, $\tilde{\kappa}_y = {}^{\kappa_y a^2}/_{u_n}$, $\tilde{\lambda}_x = {}^{\lambda_x a}/_{u_n}$, $\tilde{\lambda}_y = {}^{\lambda_y a}/_{u_n}$ and $\tilde{\overline{u}} = {}^{\overline{u}}/_{u_n}$.

$$\tilde{u}_i = \tilde{\overline{u}} + \tilde{\lambda}_x \tilde{x}_i + \tilde{\lambda}_y \tilde{y}_i + \frac{\tilde{\kappa}_x \tilde{x}_i^2}{2} + \frac{\tilde{\kappa}_y \tilde{y}_i^2}{2} \tag{12}$$

This also results in the dimensionless form of Equation-8 and Equation-9 taking the form of:

$$\tilde{u}_i = \frac{\tilde{f}_j}{\tilde{r}_{ij}}, \quad \text{for } j \neq i \tag{13a}$$
$$\tilde{u}_i = \tilde{f}_j \left[\frac{16}{3\pi} + \frac{\tilde{h}}{(1-\nu^2)} \right], \quad \text{for } j = i \tag{13b}$$

where $\tilde{f}_j = {}^{f_j}/_{f_{max}}$ is the force exerted by fibril j, relative to the local detachment force. When the model computes any $\tilde{f}_j \geq 1$, local detachment occurs so the force from these detached fibrils is re-written as $\tilde{f}_j = 0$. The stiffness matrix K_{ji} is iterated down to an $N_a \times N_a$ array, where N_a is the remaining number of attached fibrils. This new stiffness matrix is used to recalculate the force in the still attached fibrils, without the affects of the mechanical coupling between the detached fibrils and the backing layer.

By summing all dimensionless fibrillar forces and dividing by the number of fibrils, one obtains the expression for load sharing efficiency given in Equation-3. This allows for the final expression

Equation-14 below which relates load sharing efficiency to the dimensionless displacement input model.

$$\tilde{F}_{max} = \frac{\sum_{j=1}^{N} K_{ji} \tilde{u}_i}{N} \tag{14}$$

2.1.3 Correction for Finite Thickness Backing Layers

The solutions for backing layer deformation provided in Equation-13, treat the backing layer as an elastic half space that is infinitely thick and wide compared to the radius of a single fibrillar unit. In other words, $a \ll H$ & $a \ll L$ where $L = {}^{(n_x-1)d}/_2$ is considered the characteristic length of the array. This assumption is not physically accurate for the backing layers in adhesive samples utilized in prototype development. A typical adhesive sample is shown in Figure-5a, Figure-5b and Figure-6 where ${}^{L}/_{a} \approx 175$ and ${}^{H}/_{a} \approx 20$.

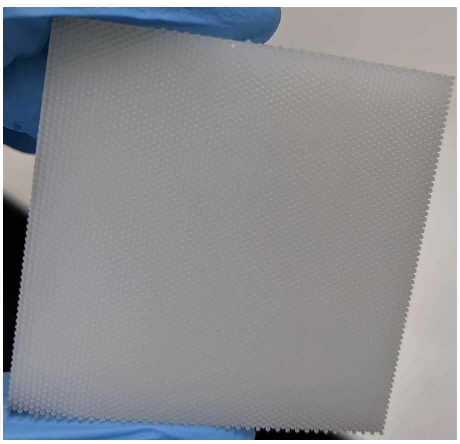

(a) Top view of an adhesive sample.

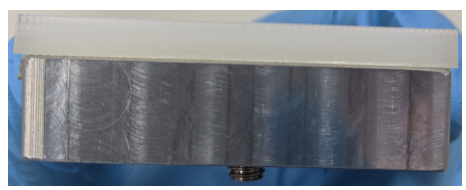

(b) Front view of an adhesive sample.

Figure 5: A typical adhesive sample utilized in prototype development.

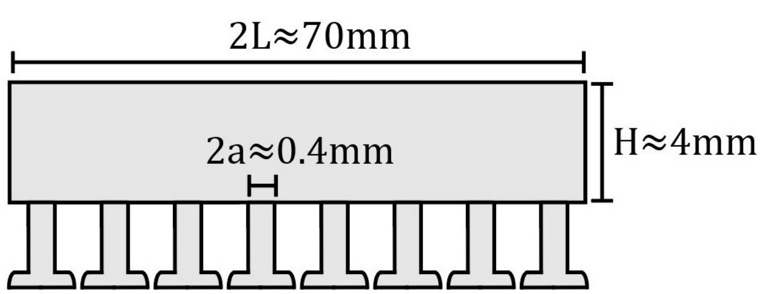

Figure 6: Labelling the physical dimensions of the adhesive sample shown in Figure-5a and Figure-5b.

To the author's knowledge, an analytical solution for non-infinite bodies has not been derived, so to correct for physical inaccuracies empirical correction factors were calculated by performing parametric studies in finite element analysis. This results in Equation-13a and Equation-13b taking on the modified forms below.

$$\tilde{u}_i = \frac{\beta \tilde{f}_j}{\tilde{r}_{ij}^{\gamma}}, \quad \text{for } i \neq j \tag{15a}$$

$$\tilde{u}_i = \tilde{f}_j \left[\frac{\alpha 16}{3\pi} + \frac{\tilde{h}}{(1-\nu^2)} \right], \quad \text{for } i = j \tag{15b}$$

The values of the correction factors were calculated using the surface level displacements experienced by BLs of varying thicknesses caused by a uniform stress σ applied over a circular region of $a =$ 0.1mm. Utilizing radial symmetry, a planar section of the backing layer was modelled in ABAQUS with $\tilde{L} = {}^{L}/{}_{a} = 175$ as shown in Figure-7. The lower face of the model was fixed from displacing along the z-axis and x-axis, while the top face acts as a free deformable surface.

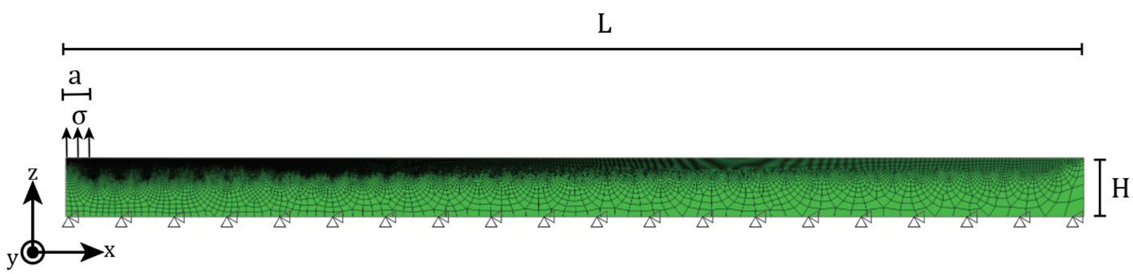

Figure 7: The boundary conditions and loading applied to the planar section model used in the finite element analysis. The model computes the dimensionless displacement $\tilde{u}_{BL}$ against radial coordinate $\tilde{r}$ at various values of dimensionless BL thickness $\tilde{H}$.

Once a dimensionless thickness $\tilde{H} = {}^{H}/{}_{a}$ is prescribed, the dimensionless displacements $\tilde{u} = {}^{u\pi E^* a}/{}_{f} = {}^{uE^*}/{}_{\sigma a}$ at the surface are calculated. These are recorded as a function of the dimensionless distance from the center of the loaded zone $\tilde{r}$. The average displacement in response to a unit force for within the loaded region of Figure-7 or $\tilde{r} \leq 1$ was calculated using trapezoidal integration and is given by Equation-16.

$$\langle \tilde{u}_{BL} \rangle = \frac{\alpha 16}{3\pi} \tag{16}$$

The parameter α is a function of the dimensionless backing layer thickness $\tilde{H}$ given by Equation-17 and plotted in Figure-8.

$$\alpha(\tilde{H}) = 1 - \frac{1}{1 + 1.232\tilde{H}^{0.809}} \tag{17}$$

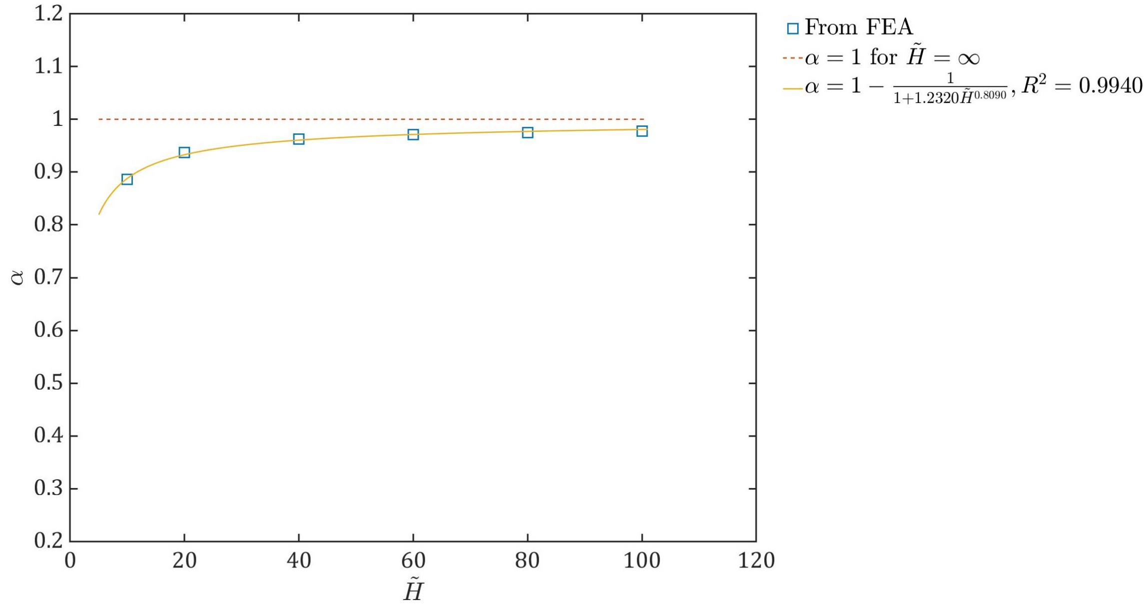

Figure 8: The fitting of the empirical correction factor α as a function of $\tilde{H}$.

The displacement in response to a unit force outside the loaded region in Figure-7 or $\tilde{r} \geq 1$ is plotted with Equation-18.

$$\tilde{u}_{BL} = \frac{\beta}{\tilde{r}^{\gamma}} \tag{18}$$

Similar to α, the parameters β and γ are functions of the dimensionless BL thickness $\tilde{H}$. Equation-19a and Equation-19b are the expressions for the parameters β and γ respectively. Figure-9a and Figure-9b show the plots for the respective parameters as well.

$$\beta(\tilde{H}) = \exp 53.15\tilde{H}^{-1.688} \tag{19a}$$

$$\gamma(\tilde{H}) = \exp 10.82\tilde{H}^{-1.065} \tag{19b}$$

As can be seen in Equation-17 and Equation-42, for the case of $\tilde{H} \to \infty$, $\alpha, \beta, \gamma = 1$. This means that Equation-15 approaches the theoretical solutions of an infinite elastic half space expressed in Equation-13.While for the opposite case of $\tilde{H} \to 0$, $\alpha = 0$ and $\beta, \gamma = \infty$ which results in $\tilde{u}_{BL} = 0$ or also known as the scenario of a rigid BL. The BL compliance that results from Equation-18 is

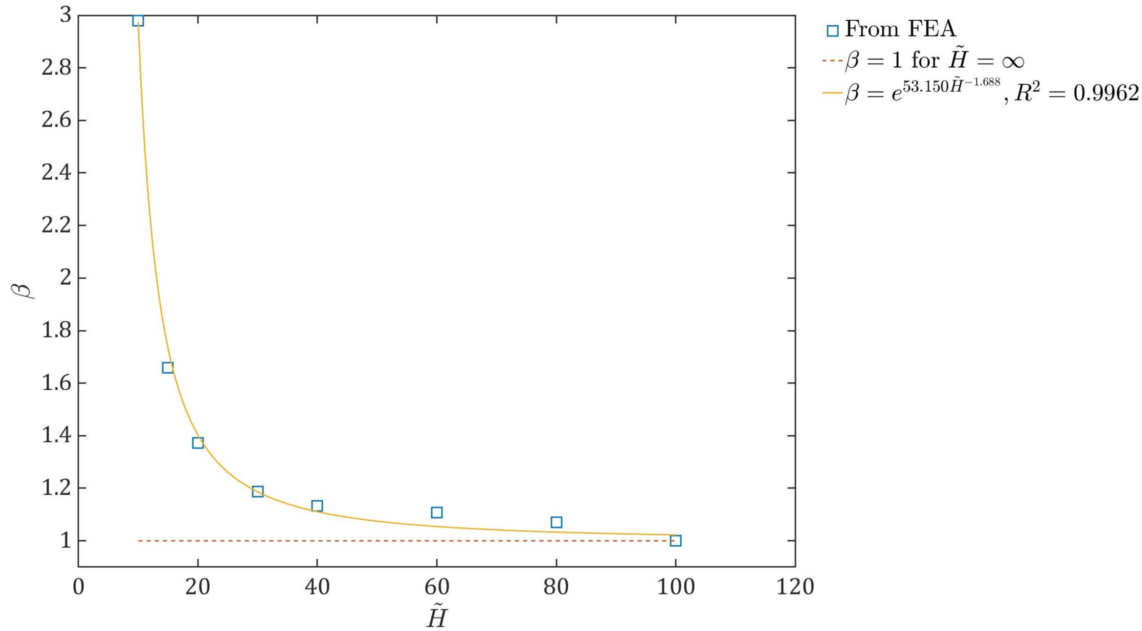

(a) The fitting of the empirical correction factor β as a function of $\tilde{H}$

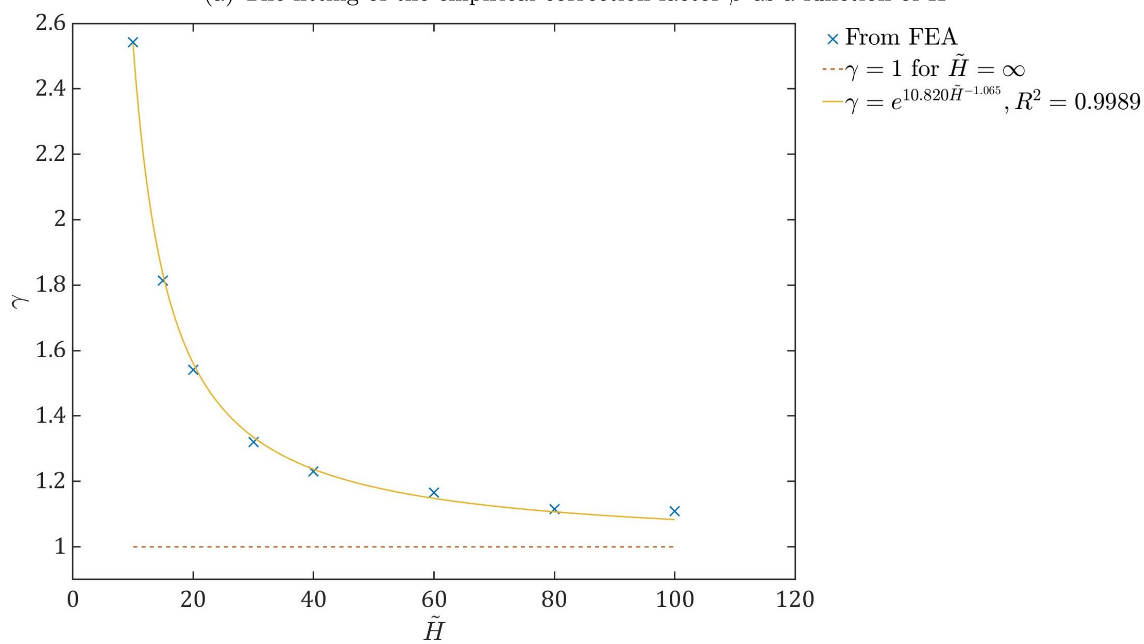

(b) The fitting of the empirical correction factor γ as a function of $\tilde{H}$

Figure 9: The fitting of the power function parameters in Equation-42

plotted as function of $\tilde{r}$ for different BL thicknesses in Figure-10.

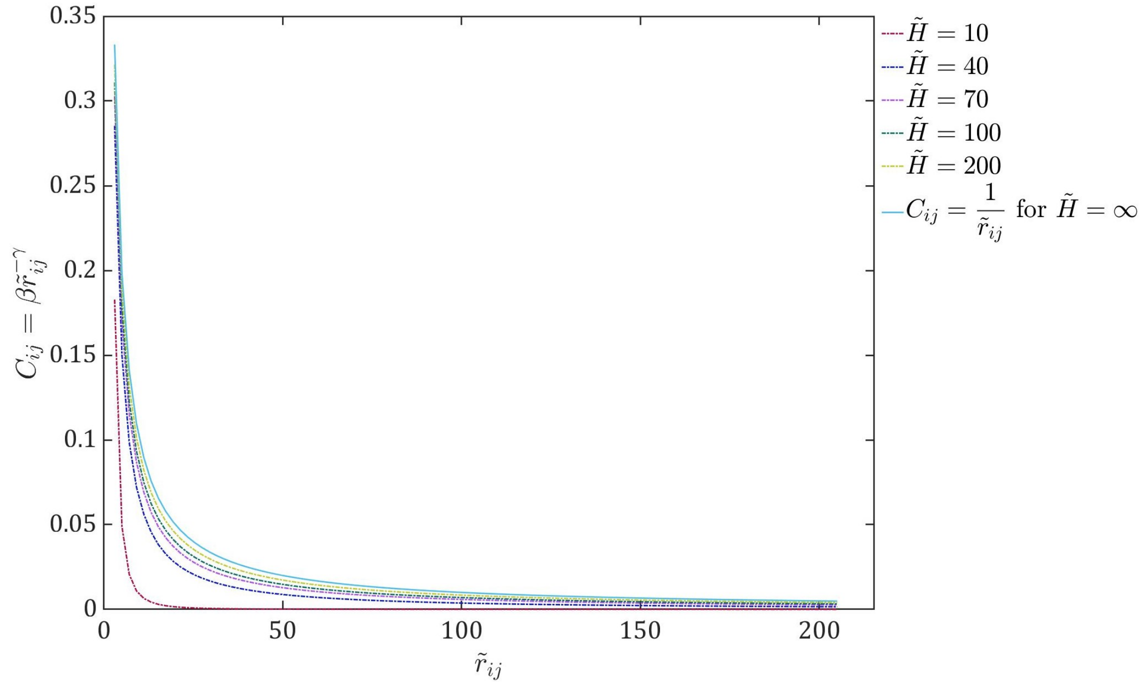

Figure 10: The value of the BL compliance as a function of $\tilde{r}$ & $\tilde{H}$ for $i \neq j$.

As for the case of a rigid BL, only fibril stretch contributes to $\tilde{u}_i$, so the compliance matrix takes the form expressed in Equation-20 where δ_{ij} is the Kronecker delta.

$$C_{ij} = \delta_{ij} \frac{\tilde{h}}{1 - \nu^2} \tag{20}$$

The width of the model was then verified to be sufficiently large by comparing the surface displacements of two models with $\tilde{L} = 175$ & $\tilde{L} = 350$ for $\tilde{H} = 10$. It was found that these displacements were identical to four decimal places for the two models, indicating that the width was large enough to not be a factor in the displacement of the BL surface.

2.1.4 Analytical Solution for Maximum Load Sharing Efficiency in the Presence of Interfacial Curvature and Misalignment

The solution for the maximum load sharing efficiency of a fibrillar array with a rigid BL was originally proposed in [35]. Here it is expanded upon to account for misalignment at the interface. For simplicity, we assume that $\tilde{\lambda}_y = \tilde{\kappa}_y = 0$. Using Equation-20, one sees that the force experienced within the fibril only depends on the tip displacement of the same fibril. Inverting and multiplying by Equation-12, one arrives at Equation-21 below.

$$\tilde{f}_i = \frac{(1-\nu^2)}{\tilde{h}}\left(\bar{\tilde{u}} + \tilde{\lambda}_x\tilde{x}_i + \frac{\tilde{\kappa}_x\tilde{x}_i^2}{2}\right) \tag{21}$$

The total dimensionless force is obtained by substituting Equation-21 into Equation-3 which results in

$$\tilde{F} = \frac{(1-\nu^2)}{\tilde{h}}\left(\bar{\tilde{u}} + \frac{1}{N}\sum_{i=1}^{N_a}\left(\tilde{\lambda}_x\tilde{x}_i + \frac{\tilde{\kappa}_x\tilde{x}_i^2}{2}\right)\right) \tag{22}$$

where N_a is the number of fibrils still attached to the RS, with $0 \leq N_a \leq N$. It has been shown in [28] that $d\tilde{F}/d\bar{\tilde{u}} < 0$ for $N_a < N$ for a rigid BL array. Hence the $\tilde{F} = \tilde{F}_{max}$ occurs when the first fibril detaches with $N_a = N$. This occurs when the RS reaches a critical separation $\bar{\tilde{u}}^*$ where a row of fibrils at $\tilde{x}_i^*$ experiences the maximum local force f_{max}. By setting $\tilde{f}_i = 1$, $\bar{\tilde{u}} = \bar{\tilde{u}}^*$ & $\tilde{x}_i = \tilde{x}_i^*$ in Equation-21, one obtains the expression for the critical separation.

$$\bar{\tilde{u}}^* = \frac{1-\nu^2}{\hat{h}} - \left(\tilde{\lambda}_x\tilde{x}_i + \frac{\tilde{\kappa}_x\tilde{x}_i^2}{2}\right) \tag{23}$$

By substituting Equation-23 into Equation-22, the expression for the maximum detachment strength as

$$\tilde{F}_{max} = 1 + \frac{(1-\nu^2)}{\tilde{h}}\left(\frac{1}{N}\sum_{i=1}^{N_a}\left(\tilde{\lambda}_x\tilde{x}_i + \frac{\tilde{\kappa}_x\tilde{x}_i^2}{2}\right) - \tilde{\lambda}_x\tilde{x}^* - \frac{\tilde{\kappa}_x\tilde{x}^{*2}}{2}\right) \tag{24}$$

For $\tilde{\kappa}_x \geq 0$, first detachment occurs at the perimeter of the adhesive. Therefor $\tilde{x}^* = \pm(n_x - 1)\tilde{d}/2$ where the sign is that of λ_x. For $\tilde{\kappa}_x < 0$, first detachment occurs near the center of the adhesive or more precisely where the maximum initial strain occurs. This is calculated by solving $\left.\frac{d\tilde{u}}{d\tilde{x}}\right|_{\tilde{x}=\tilde{x}^*} = 0$ for $\tilde{x}^*$ and rounding to the nearing value of $\tilde{x}_i$ which yields $\tilde{x}_i^*$. The expression for $\tilde{x}^*$ is shown in Equation-25 below.

$$\tilde{x}^* = -\frac{\tilde{\lambda}_x}{\tilde{\kappa}_x} \tag{25}$$

If one were to assume that $\tilde{x}^* \approx \tilde{x}_i^*$, then Equation-24 can be simplified to Equation-26. Note that the maximum value of $\tilde{x}^*$ is $\pm(n_x - 1)\tilde{d}/2$. The results of the analytical solution are compared to the numerical model in Figure-11.

$$\tilde{F}_{max}\Big|_{\tilde{\kappa}_x<0} = 1 + \frac{(1-\nu^2)}{\tilde{h}}\left(\frac{1}{N}\sum_{i=1}^{N_a}\left(\tilde{\lambda}_x\tilde{x}_i + \frac{\tilde{\kappa}_x\tilde{x}_i^2}{2}\right) + \frac{\tilde{\lambda}_x^2}{2\tilde{\kappa}_x}\right) \tag{26}$$

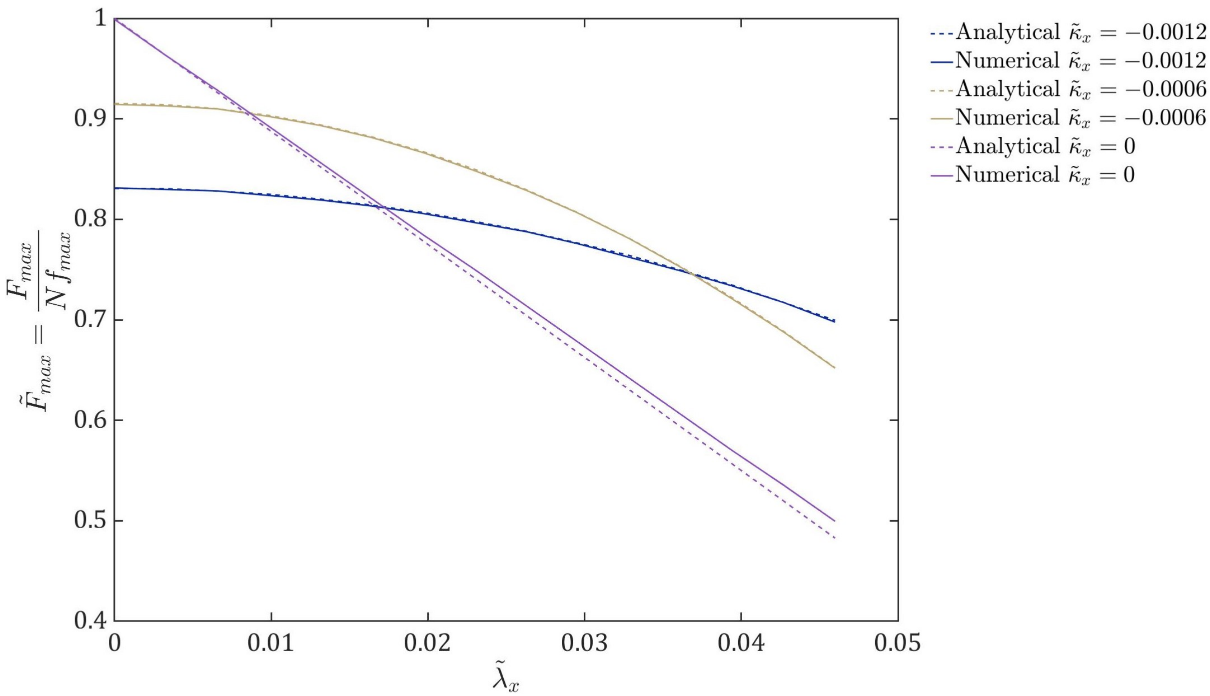

Figure 11: The results from the analytical solution in Equation-26 (dashed lines) are compared against the numerical solution (solid lines) for a fibrillar array having a rigid BL.

2.2 Numerical and Analytical Solution for Optimal Compliance Distribution

This section focuses on the numerical and analytical solutions for optimal compliance distribution throughout a fibrillar array. The section first covers the numerical compliance optimization method that was proposed by Bacca *et. al.* (2016). Then, the numerical solution is expanded upon with an asymptotic approximation that treats the array of fibrils to be a continuum of linear elastic material without any lateral load transmission (analogous to a Winkler soil). This results in the analytical solution at the end of the section.

2.2.1 Numerical Solution for Optimal Compliance Distribution

The condition of ELS is that at which each fibril tip transmits its maximum load at detachment, hence

$$f_i = f_{max} \quad \forall i \tag{27}$$

with all fibrils detaching simultaneously. This also implies that

$$u_i = \bar{u}_c + \lambda_x^d x_i \quad \forall i \tag{28}$$

where $\bar{u}_c$ is the critical prescribed separation and λ_x^d is the design misalignment. For simplicity, only misalignment in the xz-place is considered. Substituting Equation-27 and 28 into Equation-8 one obtains

$$\frac{\bar{u}_c}{f_{max}} + \frac{\lambda_x^d}{f_{max}} x_i = \frac{16}{3\pi^2 E_{BL}^* a_i} + c_i^* + \sum_{j=1, j\neq i}^{N} \frac{1}{r_{ij}} \tag{29}$$

where the optimal compliance can be expressed as

$$c_i^* = \frac{h_i}{(1-\nu^2)\pi a_i^2 E_{f,i}^*} \tag{30}$$

Equation-29 averaged over the whole array gives

$$\frac{\bar{u}_c}{f_{max}} + \frac{\lambda_x^d}{f_{max}} \frac{1}{N} \sum_{i=1}^{N} x_i = \frac{16}{3\pi^2 E_{BL}^* a_i} + c_m + \frac{1}{N} \sum_{i=1}^{N} \left(\sum_{j=1, j\neq i}^{N} \frac{1}{r_{ij}} \right) \tag{31}$$

where the average fibril compliance is

$$c_m = \frac{h}{(1-\nu^2)\pi a^2 E_f} \tag{32}$$

with h and a the mean stalk length and radius of the fibrils and E_f being the nominal value of the Young modulus. Equating Equation-29 and 31 results in

$$c_i^* = c_m + \frac{1}{\pi E_{BL}^*} \left[\frac{1}{N} \sum_{i=1}^{N} \left(\frac{16}{3\pi a_i} + \sum_{j=1, j\neq i}^{N} \frac{1}{r_{ij}} \right) - \left(\frac{16}{3\pi a_i} + \sum_{j=1, j\neq i}^{N} \frac{1}{r_{ij}} \right) + \frac{\lambda_x^d}{f_{max}} (x_i - x_m) \right] \tag{33}$$

with $x_m = {}^1/_N \sum x_i$ being the average fibril position along the x-axis. The solution proposed in Equation-33 is valid for any array shape, but comes with the computational cost of N^2 operations.

2.2.2 Asymptotic Approximation and Analytical Solution for Optimal Compliance Distribution

An array of fibrils can be considered asymptotically as a continuum of linearly elastic material without lateral load transmission. This results as BL interactions being the only mean of mechanical coupling. The contact stress σ transmitted from the RS to the BL is defined as a function of position via $\sigma(x, y)$. This stress is homogenized from the load applied to the single fibril i via the relation $\sigma(x_i, y_i) = {}^{f_i}/_{d^2}$. The accuracy of this asymptotic homogenization is inversely proportional to d. Applying the conditions of ELS at detachment, the homogeneous contact stress is calculated as Equation-34.

$$\sigma(x, y) = \frac{f_{max}}{d^2} \tag{34}$$

This principal is expanded upon to obtain a function $c^*(x, y)$.First, Equation-28 can is expressed as the displacement of the backing layer and the elongation of a fibril as shown in Equation-35.

$$\bar{u}_c = u_{BL}(x, y) + \Delta h(x, y) \tag{35}$$

The elongation of a fibril, Δh can be expressed with the optimal compliance and the force from Equation-27.

$$\Delta h(x, y) = c^*(x, y) f_{max} \tag{36}$$

where $c^*(x_i, y_i) = c_i^*$. Substituting Equation-35 into Equation- 36 one obtains

$$\frac{\bar{u}_c}{f_{max}} + \frac{\lambda_x^d}{f_{max}} x = \frac{u_{BL}(x, y)}{f_{max}} + c^*(x, y) \tag{37}$$

which can also be averaged over the area of the entire array to obtain

$$\frac{\bar{u}_c}{f_{max}} + \frac{\lambda_x^d}{f_{max}} x_m = \frac{u_{BL,m}}{f_{max}} + c_m \tag{38}$$

where $u_{BL,m} = \frac{1}{A} \int_A u_{BL}(x, y) dA$ is the average BL displacement and x_m is the x coordinate of the contact region's centroid given by $x_m = \frac{1}{A} \int_A x dA$. Next, by equating Equation-37 and Equation-38 one obtains the expression for $c^*(x, y)$ in Equation-39

$$c^*(x,y) = \frac{u_{BL,m} - u_{BL}(x,y)}{f_{max}} + c_m + \frac{\lambda_x^d}{f_{max}}(x - x_m) \tag{39}$$

2.2.3 Dimensional Analysis for Numerical Solution

Equation-33 is divided by c_m to obtain

$$\frac{c_i^*}{c_m} = 1 + \frac{\rho R E_f}{h E_{BL}^*}(\Psi_m - \Psi_i) + \lambda_x^d\Big(\frac{x_i - x_m}{\Delta h_m}\Big) \tag{40}$$

where

$$\rho = \frac{\pi a^2}{d^2} \tag{41}$$

is the fibril stalk density and

$$\Psi_i = \frac{\Gamma R}{N}\left(\frac{16}{3\pi a_i} + \sum_{j=1, j\neq i}^{N} \frac{1}{r_{ij}}\right) \tag{42a}$$

$$\Psi_m = \frac{1}{N}\sum_{i=1}^{N} \Psi_i \tag{42b}$$

are factors that depend on the position of the fibril within the array. Furthermore the parameter Γ is a geometrical factor associated with the array shape and is defined in Equation-43.

$$\Gamma = \frac{Nd^2}{\pi R^2} \tag{43}$$

Note that R is the characteristic length of the contact area with $R = {}^{(n_x-1)d}/_{2}$. Finally Δh_m is the average fibril elongation at detachment and is expressed in Equation-44.

$$\Delta h_m = c_m f_{max} \tag{44}$$

For dense arrays with a large number of fibrils, one can assume $A \simeq Nd^2$ resulting in $\Gamma \simeq 1$ when the array is circular and $\Gamma \simeq {}^4/_{\pi}$ when the array is a square.

2.2.4 Dimensional Analysis for Analytical Solution

The optimal compliance in Equation-39 can be re-written as relative to the average compliance as shown in Equation-45. Note that where E_f is the average fibrillar Young's modulus.

$$\frac{c^*(x,y)}{c_m} = 1 + \frac{\rho R E_f}{h E^*_{BL}}\left(\tilde{u}_{BL,m} - \tilde{u}_{BL}(x,y)\right) + \frac{\lambda^d_x}{\Delta h_m}(x - x_m) \tag{45}$$

where the variable $\tilde{u}_{BL}$ is shown in Equation-46.

$$\tilde{u}_{BL} = \frac{E^*_{BL} d^2}{f_{max} R} u_{BL} \tag{46}$$

3 Results

3.1 Interfacial Curvature in Finite Thickness Backing Layers

3.1.1 The Effect of Curvature in Finite Thickness BL Arrays

The evolution of $\tilde{F}$ versus $\tilde{\tilde{u}}$ for two adhesives with $\tilde{H} = 15$ and $\tilde{H} = 40$ is shown in Figure-12 below. Both adhesives have $N = 1024$ fibrils with $\tilde{h} = \tilde{d} = 5$ and $\tilde{\lambda}_x = \tilde{\lambda}_y = 0$. The curvature $\kappa_y = 0$ while κ_x changes from $-0.0006, 0$ & 0.0006. A positive curvature increments the stretch of peripheral fibrils (Figure-4), hence increases load concentration at the edge of the array. This effect superposes to that of BL interaction and prompts earlier detachment of the adhesive, compared to a system with no curvature. This in agreement with Figure-12, where $\kappa_x > 0$ results in a lower $\tilde{F}_{max}$ compared to $\kappa_x = 0$. Conversely, a negative curvature counteracts the load concentrations created by BL interactions, thereby generating higher strength. Figure-12 reports higher $\tilde{F}_{max}$ for $\tilde{\kappa}_x < 0$ than for $\tilde{\kappa}_x = 0$.

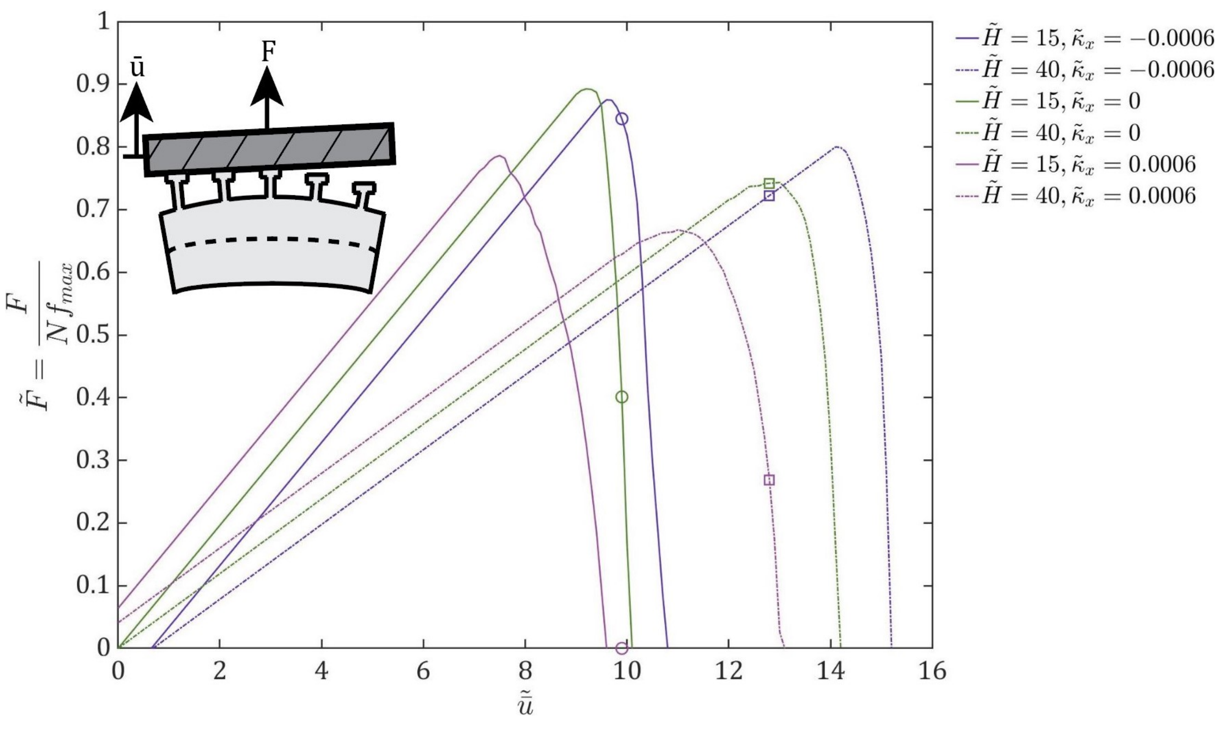

Figure 12: Dimensionless force $\tilde{F}$ versus displacement $\tilde{\tilde{u}}$ for a fibrillar adhesive having $N = 1024, \tilde{\lambda}_x = \tilde{\lambda}_y = 0, \tilde{H} = 15$ and $\tilde{H} = 40$ and three values of $\tilde{\kappa}_x$ as indicated. Circular markers correspond to $\tilde{\tilde{u}} = 9.9$ which is the point of detachment for $\tilde{\kappa}_x = 0$ and $\tilde{H} = 15$, while square markers correspond to $\tilde{\tilde{u}} = 12.8$, the point of detachment for $\tilde{\kappa}_x = 0$

Figure-12 also reports square marks in the three force-displacement curves of $\tilde{H} = 40$ at $\tilde{\tilde{u}} = 12.8$, which is the critical separation generating the peak force for $\tilde{\kappa}_x = 0$. The circle markets in the three force-displacement curves of $\tilde{H} = 15$ at $\tilde{\tilde{u}} = 9.9$ which is a post peak force separation. The fibril stretch and load distribution occurring within the array configurations associated with the square and circle marks are visualized Figures-13,14.

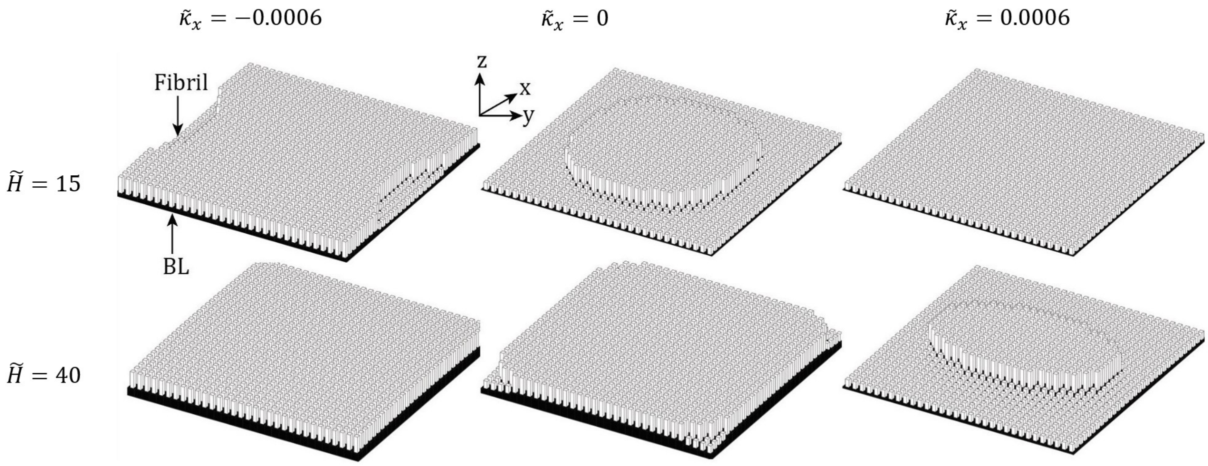

Figure 13: Dimensionless force $\tilde{F}$ versus displacement $\tilde{\tilde{u}}$ for a fibrillar adhesive having $N = 1024, \lambda_x = \lambda_y = 0$.

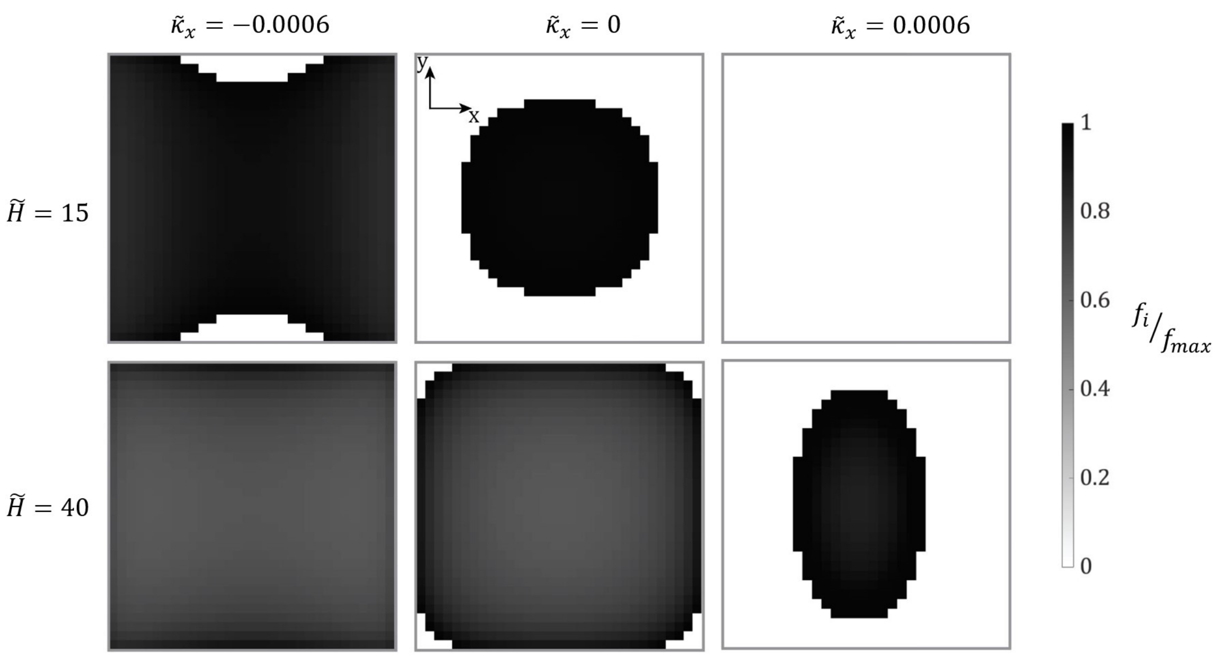

Figure 14: Dimensionless force $\tilde{F}$ versus displacement $\tilde{\tilde{u}}$ for a fibrillar adhesive having $N = 1024, \lambda_x = \lambda_y = 0$.

Figure-15 correlates the dimensionless detachment strength $\tilde{F}_{max}$ with BL thickness $\tilde{H}$, for various curvatures $\tilde{\kappa}_x$. The adhesive has $N = 2500$, $\tilde{h} = \tilde{d} = 5$, and we adopt $\tilde{\lambda}_x = \tilde{\lambda}_y = 0$ and $\tilde{\kappa}_y = 0$. As previously observed [28], a thick BL reduces the detachment strength of the adhesive in the absence of interfacial misalignment, while a thinner one provides higher strength due to a reduced BL interaction. As deduced from Figure-15, the curvature-induced strengthening observed in the previous figures applies only for relatively thick BL. Conversely, for thin BL negative curvature results in strength reduction. This is due to the proportionality of BL interaction with $\tilde{H}$. BL interaction produces load concentration to the peripheral fibrils, while negative curvature concentrates the load to the center of the adhesive. The interplay between these competing phenomena defines the load share within the array, and if one prevails the other, the result is a greater non-uniformity in load sharing with consequent strength reduction.

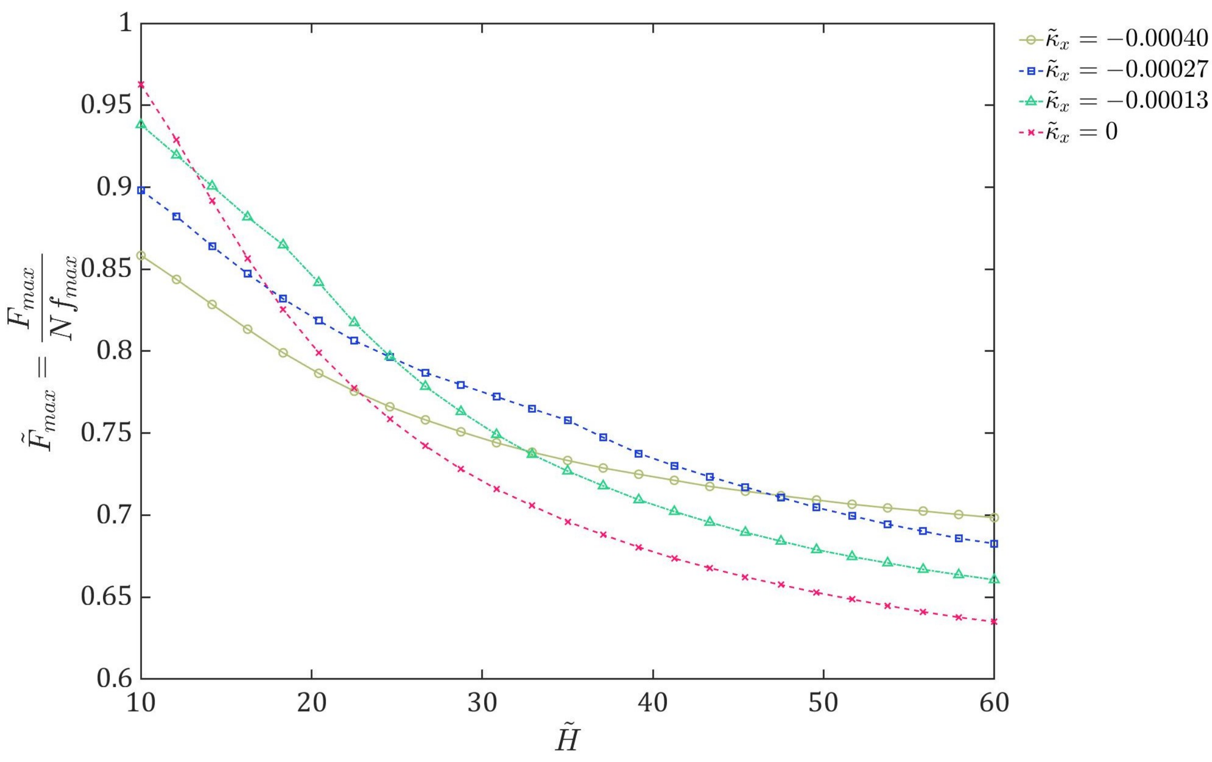

Figure 15: The load sharing efficiency of arrays with constant $\tilde{\kappa}_x$ and increasing BL thickness. The arrays have characteristics $N = 2500$ and $\tilde{h} = \tilde{d} = 5$

Figure-16 correlates $\tilde{F}_{max}$ with $\tilde{\kappa}_x$, for various combinations of $\tilde{d}, \tilde{h}, andN$. The adhesive has $\tilde{H} = 25$ and we adopt $\tilde{\lambda}_x = \tilde{\lambda}_y = 0$, and $\tilde{\kappa}_y = 0$. A positive $\tilde{\kappa}_x = 0$ always reduces $\tilde{F}_{max}$ because the edge load concentration created by positive curvature, from Equation-12, amplifies that created by BL interaction. The sensitivity of $\tilde{F}_{max}$ with respect to $\tilde{\kappa}_x$ is proportional to $\tilde{d}$ and N because both contribute to an enlargement of the fibrillar array and hence on the load concentration created by curvature. Because $\tilde{h}$ is proportional to the compliance of each fibril, larger $\tilde{h}$ creates a reduction in BL interaction and mitigates the effect of load concentration created by interfacial curvature. This is because more compliant fibrils are less sensitive to non-uniform stretch and hence less likely to create a significant load concentration. A negative $\tilde{\kappa}_x = 0$ gives better strength up to peak, and then begins to reduce it. The benefits in strength are created by a load concentration at the center of the adhesive, from Equation-12, which counteracts the edge load concentration created by BL interaction. An excessive curvature-induced load concentration overcomes BL interaction and prompt early detachment of the central fibrils, thereby reducing the adhesive strength. The load concentration is again proportional to $\tilde{d}$ and N, due to an increased array size, and to $1/\tilde{h}$ due to a better tolerance of each fibril to differential stretch. The strength peak from negative curvature, evidenced for $\tilde{d} = 7$, occurs at the critical curvature $\tilde{\kappa}_x^*$, which modulus is inversely proportional to $\tilde{d}$ and N, while appears to be indifferent to $\tilde{h}$.

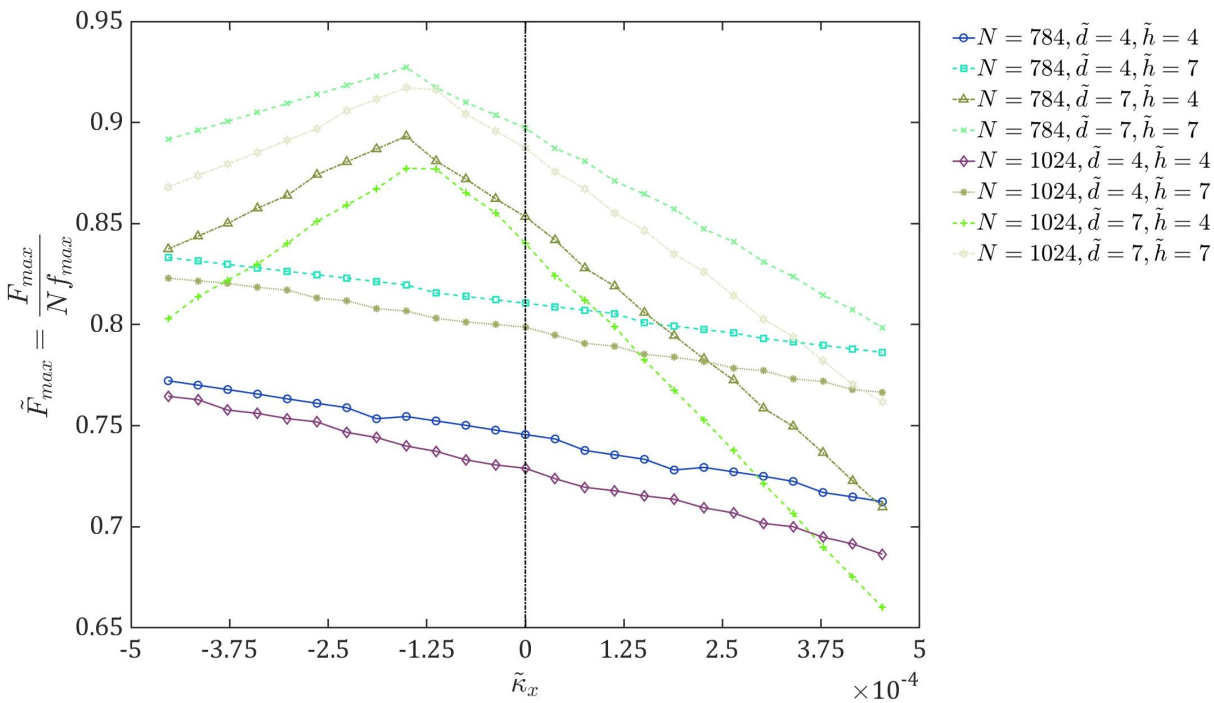

Figure 16: The dimensionless detachment strength $\tilde{F}_{max}$ versus curvature $\tilde{\kappa}_x$ for adhesives of various number of fibrils N, dimensionless fibril length $\tilde{h}$ and spacing $\tilde{d}$. For all curves $\tilde{H} = 25$, $\tilde{\lambda}_x = \tilde{\lambda}_y = 0$ and $\tilde{\kappa}_y = 0$.

Figure-17 correlates $\tilde{F}_{max}$ with $\tilde{\lambda}_x$ for various combinations of $\tilde{\kappa}_x$ and $\tilde{H}$. The adhesive has $N = 900$, $\tilde{d} = \tilde{h} = 5$ and $\tilde{\lambda}_y = \tilde{\kappa}_y = 0$. For $\tilde{H} = 0$ we used the analytical solution provided in Appendix B, for an adhesive having a rigid BL. Negative curvature has proven to strengthen the adhesive, within the limitations dictated by $N, \tilde{d}, \tilde{h}$ & $\tilde{H}$, while misalignment has shown to reduce detachment strength [28]. From Figure-17 we can observe that a negative $\tilde{\kappa}_x$ always reduces the sensitivity of $\tilde{F}_{max}$ to $\tilde{\lambda}_x$ for any $\tilde{H}$. Negative curvature, hence, mitigates the load concentration created by misalignment for any BL thickness. The reduced sensitivity produces a higher adhesive strength when $\tilde{\lambda}_x$ is larger than a threshold, which is proportional to the modulus of $\tilde{\kappa}_x$, and $^1/_{\tilde{H}}$. This is due to the interplay between the center load concentration created by the negative curvature, the edge load concentrations created by BL interaction, and that created by misalignment. Because a positive curvature would only superpose to misalignment and further reduce strength, in this figure we only explore the interplay between misalignment and negative curvature.

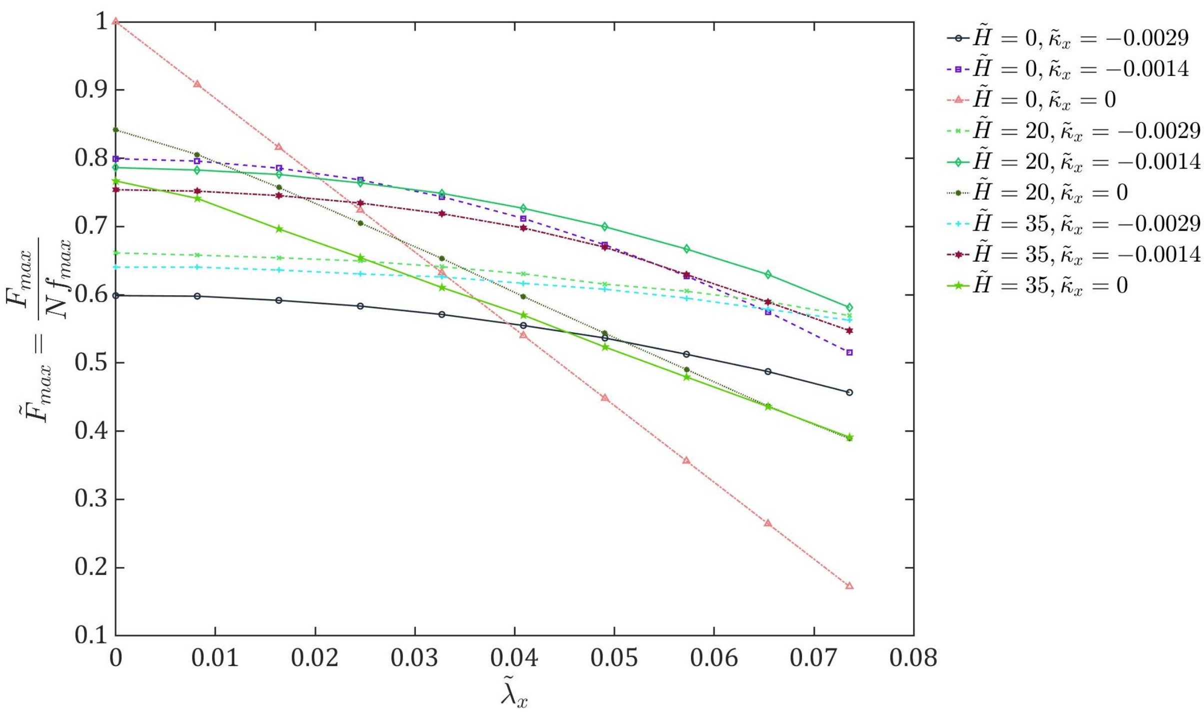

Figure 17: Comparing load sharing efficiency against misalignment angles for arrays of varying BL thickness and curvature. Each array has the constant parameters $N = 900$, $\tilde{d} = 5$, and $\tilde{5}$.

In Figure-18 the sensitivity to misalignment of finite thickness BL arrays is compared to the two simplified cases of a rigid BL and an infinite elastic half space. Neither of the cases of $\tilde{H} = 30$ or $\tilde{H} = 15$ are not accurately represented by the assumption of a rigid BL. Significant discrepancy in strength occurs at small misalignment angles as well as in the sensitivity to misalignment itself. The arrays with $\tilde{H} = 200$ and $\tilde{H} = 300$ demonstrate how thick of BL is necessary for the assumption of an infinite elastic half space to be applicable.

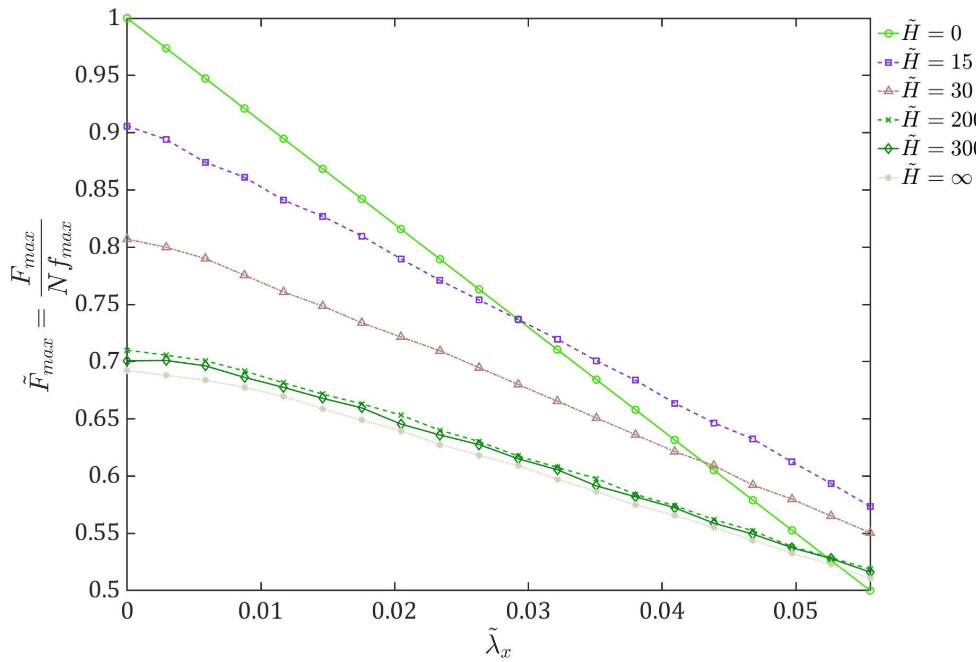

Figure 18: Dimensionless force $\tilde{F}$ versus displacement $\tilde{\tilde{u}}$ for a fibrillar adhesive having $N = 1024, \lambda_x = \lambda_y = 0$.

In Figure-19 the average detachment strength for arrays with varying amounts of fibril defects is is plotted against BL thickness. The average detachment strength was calculated by performing a Monte-Carlo simulation that treated fibril heights as a stochastic property modulated about an intended mean of $\langle h \rangle = 5$. The randomly distributed offset in fibril height influences both the pre-loading experienced by the fibrils and the compliance of the fibril itself. The variance in fibril height within a sample is denoted as s_h^2 and 50 trials are run for each combination of s_h^2 and $\tilde{H}$. For thin backing layers, there is a greater sensitivity to non-uniform fibril height and compliance. The drop in average load sharing capability becomes more significant as the variability in height and compliance increases. As the BL thickness increases, the drop off in average ultimate strength decreases which is due to the increased BL compliance being able to mitigate pre-loading and varying fibril compliance. Although more uniform arrays show the greatest sensitivity to increases in BL compliance, the effect plateaus as $\tilde{H}$ increases. The curves of $s_h^2 = 0.15, 0.225$ and 0.3 display inflection points at $\tilde{H} \approx 11.67, 13.34$ and 15 where the plateauing begins. The inflection point acts as a bounding between the array's compliance being predominantly controlled by fibril length or the BL.

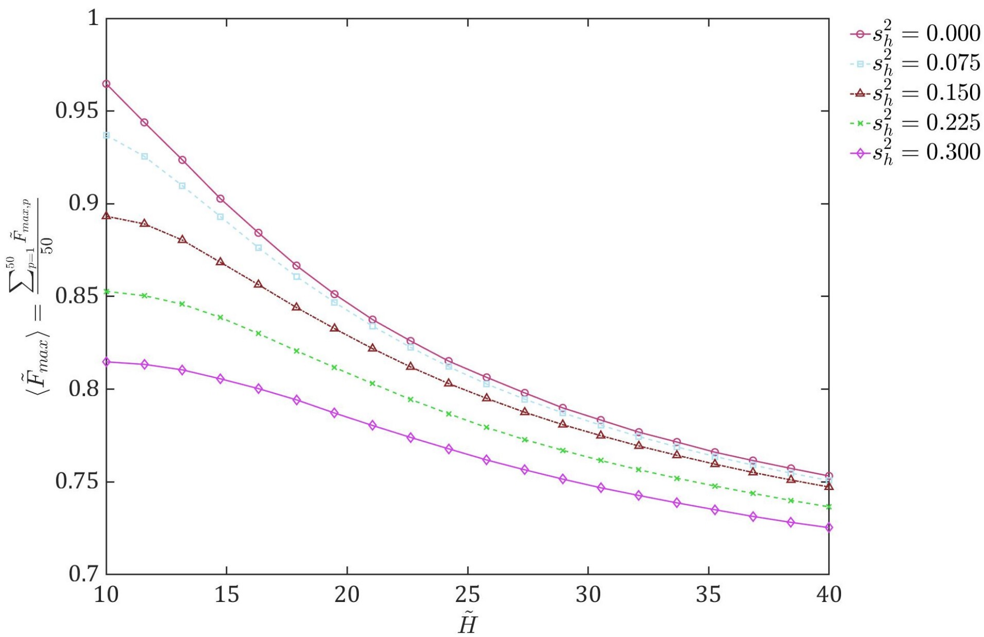

Figure 19: Dimensionless force $\tilde{F}$ versus displacement $\tilde{\bar{u}}$ for a fibrillar adhesive having $N = 1024, \lambda_x = \lambda_y = 0$.

3.1.2 Discussion

The model is based on linear elasticity, which relies on the hypothesis of small strain and small displacements. This hypothesis is satisfied if the pull-off strength of each fibril is sufficiently small to ensure small displacements overall in the adhesive. In the case of significant adhesion forces, the adhesive might experience significant strain. In this case, our model only provides a first-order estimation of the detachment strength. Additionally, the model considers quasi-static detachment. I.e. it neglects the rate-dependent behavior of the material composing the adhesive. Our hypothesis is satisfied if the velocity of BL-RS separation, $d\bar{u}/dt$, is negligible compared to the ratio between the fibril length, h, and the relaxation time, t_r.

[24] explored the effect of BL thickness, H, through experiments and compared their results with the two aforementioned extreme cases. The case of a rigid BL corresponds to that at which $H = 0$. In this case, the fibrillar adhesive exhibits no BL interaction and the displacement of the fibrils' tip

is only due to fibril stretch. The case of a BL considered to be an elastic half space corresponds to that at which $H = \infty$. In many engineering prototypes as well as in nature, the BL has a thickness that is comparable to the size of the fibrillar interface, hence one needs to extend the model by [28] to account for the influence of H on BL interaction quantitatively for the general case of $0 < H < \infty$. The correctional terms in Equation-19a and 19b, where the second term on the right-hand side relies on the description of the displacement field surrounding the region of fibrillar protrusion with a power-law function, as detailed in Section-2.1.3. This approximation provides good accuracy for large BL thickness, while introduces significant error when $\tilde{H} < 10$. A more sophisticated law can provide better accuracy for a very thin BL.

In Equation-12, the influence of interfacial curvature between the adhesives and the RS with a quadratic function of the fibril position in the array. This expression is accurate only in the case of small curvatures, i.e when $\kappa_x L_x \ll 1$, with $L_x = {}^{(n_x-1)d}/_2$ the size of the contact region along the x-axis.

3.2 Analytical Solution for Compliance Optimization

3.2.1 Solution for a Circular Array of Fibrils

This section will demonstrate the solution for Equation-45 for thee case of a fibrillar adhesive in the form of a circular array. Since misalignment in an application can be indeterminable in magnitude and sign, the design misalignments of $\lambda_x^d = 0$ will be imposed. This will guarantee ELS for any case with $\lambda_x = 0$ and improve load sharing for $\lambda_x \neq 0$ [28]. Using the contact mechanics solution from [34], Equation-46 takes the form of

$$\tilde{u}_{BL} = \frac{4}{\pi} \breve{E}\left(\frac{r}{R}\right) \tag{47}$$

where x and y are replaced by r, thanks to radial symmetry and $R = L$. In Equation-47 $\breve{E}(\frac{r}{R}) = \int_0^{\pi/2} \sqrt{1 - ({}^{r \sin\theta^*}/_R)^2} d\theta^*$ is the complete elliptical integral of the second kind and θ^* being an integration variable. Equation-45 becomes

$$\frac{c^*(\tilde{r})}{c_m} = 1 + \frac{\rho E_f 4R}{E_{BL}^* \pi h}\left[\breve{E}_m - \breve{E}(\tilde{r})\right] \tag{48}$$

where $\tilde{r} = {}^{r}/_{R}$ and $\breve{E}_m = 2\int_0^1 \breve{E}(\tilde{r})\tilde{r}d\tilde{r}$ due to radial symmetry.

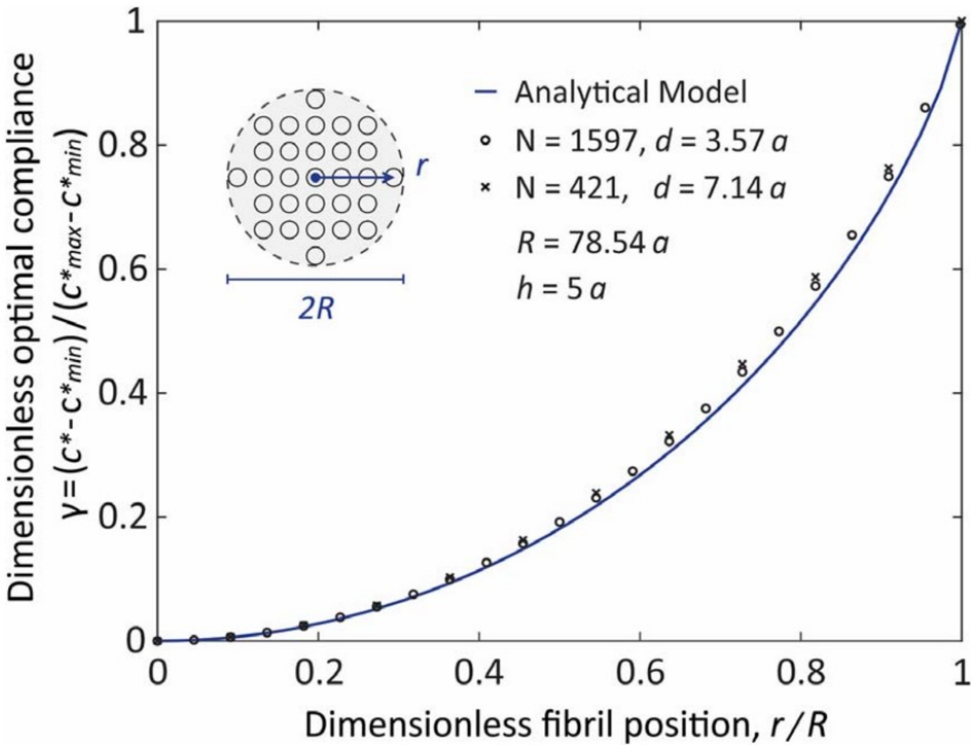

Figure 20: Optimal compliance distribution for fibrils in a circular array of radius R. Crosses and circles indicate the solution obtained with the numerical method from [28], while the solid line reports the results from the proposed analytical model from Equation-48.

The optimal compliance given by the numerical method and Equation-45 are generally maximum at the perimeter of the contact region and minimum at the center. Identifying the former with c^*_{max} and the latter with c^*_{min}, the geometrical distribution of fibril compliance in dimensionless form using Equation-49 in Figure-20.

$$\gamma_c = \frac{c^* - c^*_{min}}{c^*_{max} - c^*_{min}} \tag{49}$$

In Figure-20 the solid line indicates the results obtained from the proposed asymptotic solution at Equation-48, while the symbols indicate the results obtained from [28]. Parameters of the array were set to $E_f = E$, $\nu = 0.5$, $R = 78.54a$, and $h = 5a$. For the numerical analyses, the cases of $d = 3.57a$ and $N = 1597$ giving $\rho = 0.25$ from Equation-41 as well as $d = 7.14a$ and $N = 421$ giving $\rho = 0.06$. An increase in accuracy is shown as the fibril density ρ increases.

3.2.2 Asymptotic Solution for Compliance Optimization in Rectangular Arrays

For a rectangular array with dimensions $2L$ by $2l$ with the aspect ratio $\eta = {}^{l}/_{L}$ ($\eta \geq 1$), Equation-45 becomes Equation-50

$$\tilde{u}_{BL}(x, y) = \frac{1}{\pi}\phi\Big(\frac{x}{L}, \frac{y}{l}\Big) \tag{50}$$

where

$$\begin{aligned}
\phi(\hat{x}, \hat{y}) = (\hat{x}+1)\ln&\left[\frac{\eta(\hat{y}+1) + \sqrt{\eta^2(\hat{y}+1)^2 + (\hat{x}+1)^2}}{\eta(\hat{y}-1) + \sqrt{\eta^2(\hat{y}-1)^2 + (\hat{x}+1)^2}}\right]\\
+\,\eta(\hat{y}+1)\ln&\left[\frac{(\hat{x}+1) + \sqrt{\eta^2(\hat{y}+1)^2 + (\hat{x}+1)^2}}{(\hat{x}-1) + \sqrt{\eta^2(\hat{y}+1)^2 + (\hat{x}-1)^2}}\right]\\
+\,(\hat{x}-1)\ln&\left[\frac{\eta(\hat{y}-1) + \sqrt{\eta^2(\hat{y}-1)^2 + (\hat{x}-1)^2}}{\eta(\hat{y}+1) + \sqrt{\eta^2(\hat{y}+1)^2 + (\hat{x}-1)^2}}\right]\\
+\,\eta(\hat{y}-1)\ln&\left[\frac{(\hat{x}-1) + \sqrt{\eta^2(\hat{y}-1)^2 + (\hat{x}-1)^2}}{(\hat{x}+1) + \sqrt{\eta^2(\hat{y}-1)^2 + (\hat{x}+1)^2}}\right]
\end{aligned} \tag{51}$$

where $\hat{x} = {}^{x}/_{L}$ and $\hat{y} = {}^{y}/_{L\eta}$. Substituting Equation-50 into Equation-45

$$\frac{c^*(x, y)}{c_m} = 1 + \frac{\rho E_f L}{E^*_{BL}\pi h}\left[\phi_m - \phi\big(\frac{x}{L}, \frac{y}{L\eta}\big)\right] \tag{52}$$

with $\phi_m = \int_0^1\int_0^1 \phi(\hat{x}, \hat{y})d\hat{x}d\hat{y}$.

Figure -21 reports the solution of Equation-52 (crosses and circles) and compares it to the numerical solution from [28] (solid line) for a square array. In this case, it was assumed $E_f = E$, $\nu = 0.5$, $R = 71.4a$, and $h = 5a$. For the numerical analyses, the cases of $d = 3.57a$ and $N = 1681$ giving $\rho = 0.25$ as well as $d = 7.14a$ and $N = 441$ giving $\rho = 0.06$. Also in this case, the accuracy increases, as the fibril density ρ increases.

In Figure-22, the force-versus-separation plot in dimensionless form for a circular and a square array with uniform compliance (solid lines) and with optimal compliance distribution, from Equation-48 and Equation-52, respectively, and same contact area (dashed lines). The parameters that were used in the simulations to generate Figures-20 and 21 are used again, however only with the highest

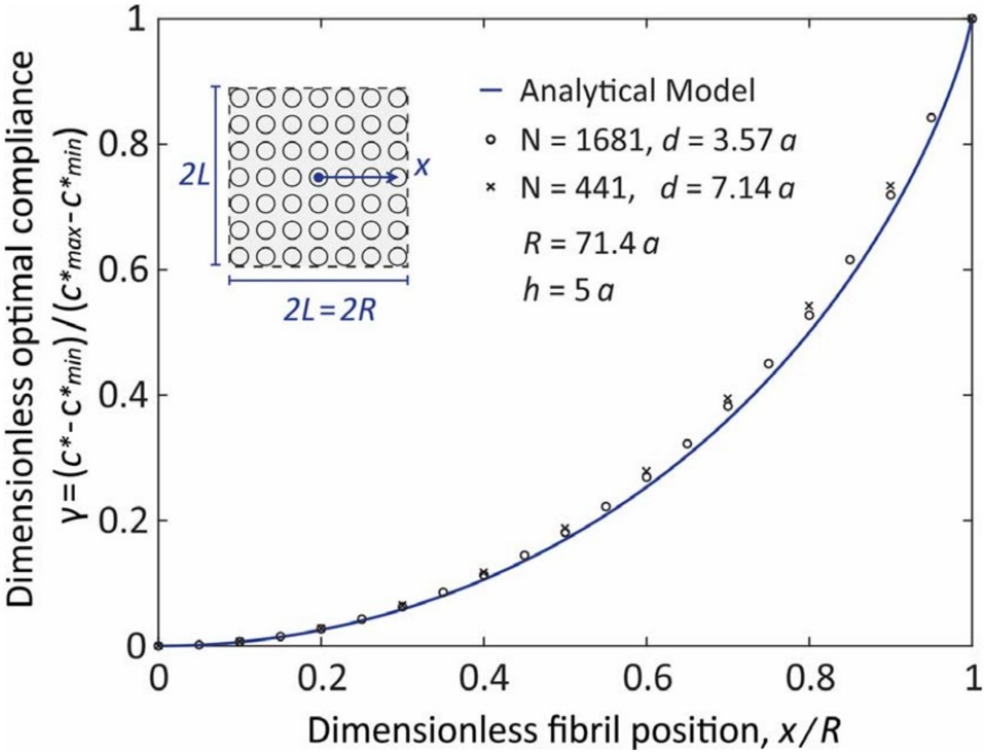

Figure 21: Optimal compliance distribution for fibrils in a square array of size $2L$. Crosses and circles indicate the solution obtained with the numerical method from [28], while the solid line reports the results from the proposed analytical model from Equation-52

N. The arrays having uniform compliance detach earlier and do not achieve ELS. Furthermore, the fibrils detach rapidly but not simultaneously once first detachment has occurred. The arrays with optimal compliance distribution instead obtain ELS reaching nearly maximum theoretical strength, with $F_{max} \approx N f_{max}$.

Figure-23 and Figure-24 show the distribution of fibril forces as well as the deformation of the fibrils and BL for various cases taken from the simulations in Figure-22 (circles and squares overlaid to the plots). Figure-23 shows the case of the circular array while Figure-24 shows that of a square array. Both figures compare the case of uniform compliance distribution (left) with that of optimal compliance distribution (right). In this comparison, we keep the same separation $\bar{u}$ for uniform compliance and optimal compliance.

3.2.3 Optimized Load Sharing in the Presence of Misalignment

Figure-25 reports the normalized detachment force (or adhesive strength) in the presence of misalignment for circular arrays (black lines) and square arrays (blue lines) optimized with the numerical

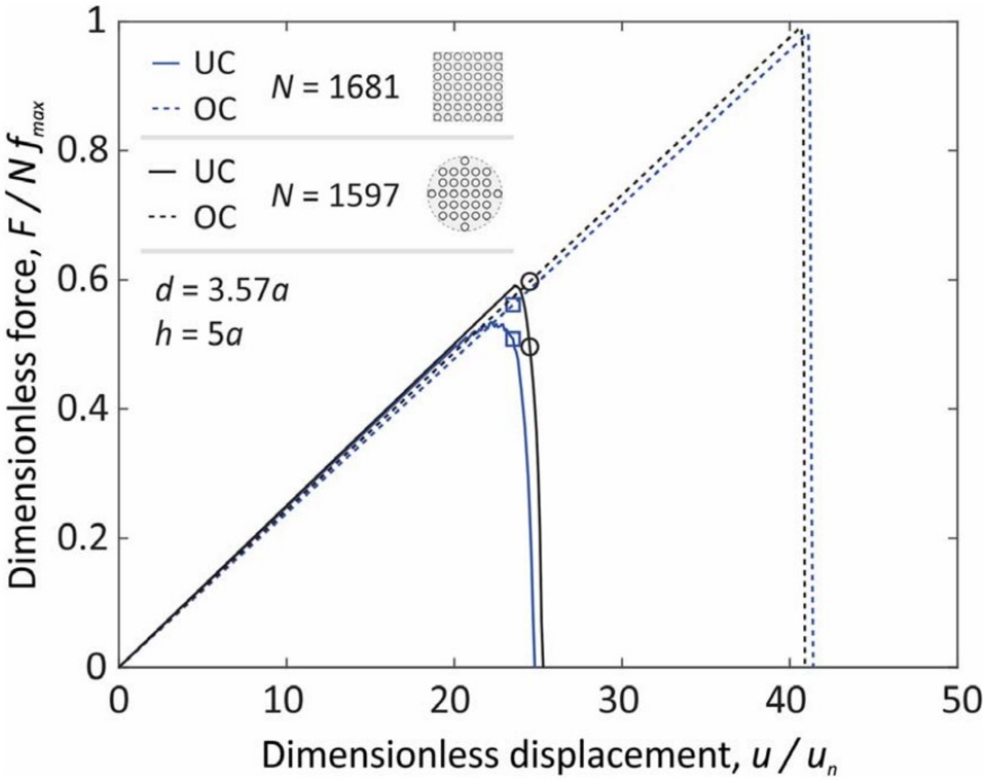

Figure 22: Force versus displacement during detachment for a fibrillar adhesive having circular (black) and square (blue) array. Fibrils with uniform compliance (UC, solid lines) and optimal compliance (OC, dashed lines) are compared. The hollow circle and square markers indicate the configuration shown in Figure-23 and Figure-24 respectively.

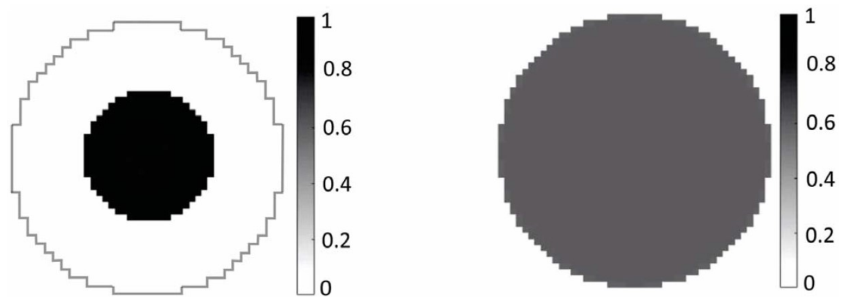

(a) Fibrillar force distribution f_i/Nf_{max} at $\bar{u}/u_n = 24.5$.

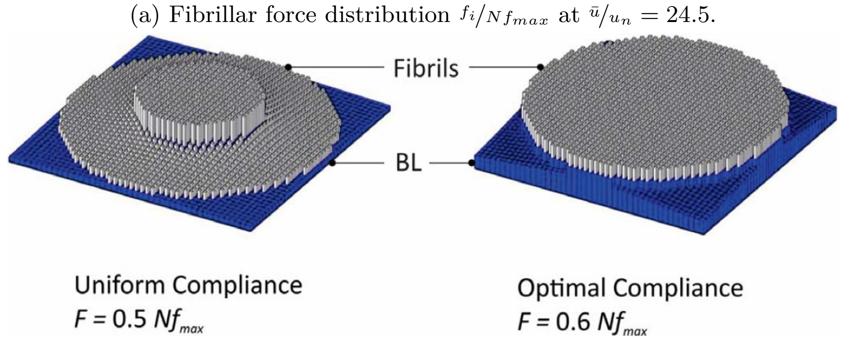

(b) Deformation

Figure 23: Adhesive configuration, inters of (a) fibrillar force distribution and (b) BL and fibril deformation, for a circular array with uniform (left) and optimal (right) compliance distribution, from the analysis in Figure-22.

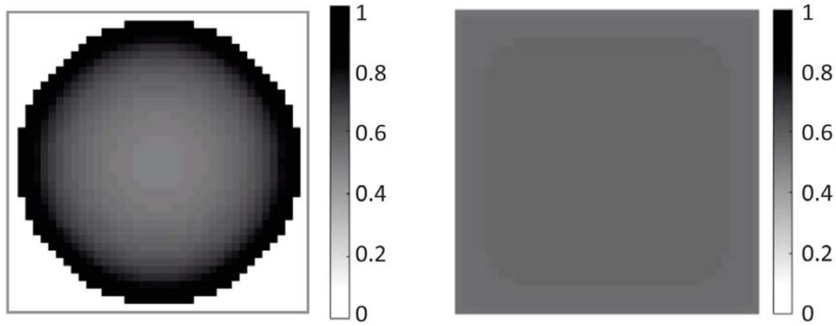

(a) Fibrillar force distribution ${}^{f_i}/_{Nf_{max}}$ at ${}^{\bar{u}}/_{u_n} = 23.5$.

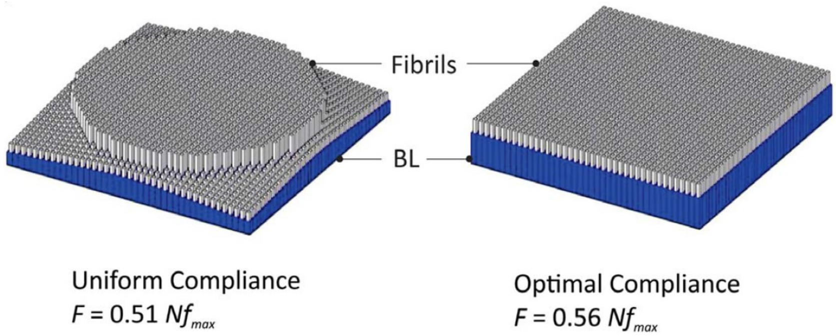

(b) Deformation

Figure 24: Adhesive configuration, inters of (a) fibrillar force distribution and (b) BL and fibril deformation, for a square array with uniform (left) and optimal (right) compliance distribution, from the analysis in Figure-22.

solution from [28] (dashed lines) and with the proposed analytical solution from Equation-45 (solid lines). In this figure, we use the same parameters used in Figure-22 but the different number of fibrils.The normalized detachment force, ${}^{F_{max}}/_{Nf_{max}}$, can be used as a measure of the load sharing efficiency of the array. In our analysis, we only consider positive misalignment θ; however, the results reported can be easily extended to negative misalignments in force of the symmetry of the problem given by $\theta_d = 0$. For both circular and square arrays, the numerical solution produces higher adhesive strength, compared with the analytical solution, for relatively small misalignments. For misalignments that are larger than a transition value θ_{tr}, the analytical solution outperforms the numerical one, evidencing a benefit from the asymptotic approximation in the case of significant statistical misalignment ($|\theta| > |\theta_{tr}|$). θ_{tr} is a function of the parameters defining the array, namely, number of fibrils N, fibril spacing d and the average fibril length h. This is because the numerical solution is exact and hence will be inherently more sensitive to unintended variations at the interface. In Figure-25, the transition misalignment is $\tan\theta_{tr} = 0.006$ for the circular array and $\tan\theta_{tr} = 0.021$ for the square array. For both square and circular arrays, the adhesive strength produced with numerical optimization appears to be more sensitive to misalignment, compared with the strength produced by the proposed analytical solution.

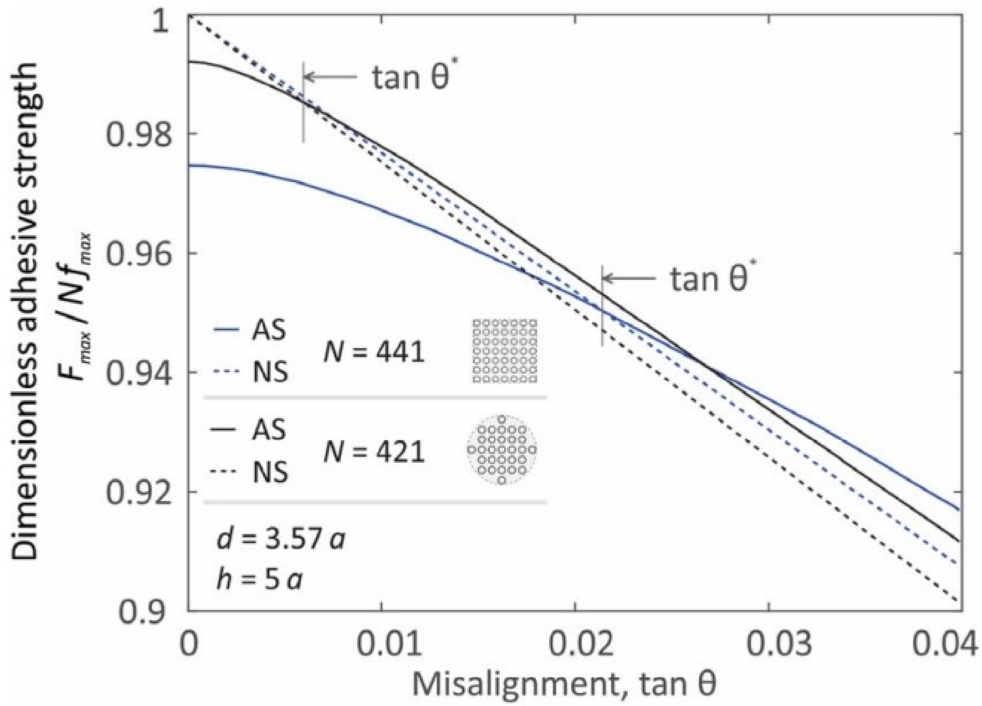

Figure 25: Evolution of the dimensionless adhesive strength for increasing misalignment of arrays having optimal fibril compliance distribution. We consider square arrays (blue lines) and circular arrays (black lines) optimized with the numerical solution (NS, dashed lines), from [28] and with the proposed asymptotic solution (AS, solid lines), from Equation-48 and Equation-52.

3.2.4 Optimized Load Sharing in the Presence of Fibrillar Defects

To validate the proposed theory and test the robustness of the optimization in compliance distribution among fibrils, a Monte Carlo simulation was conducted. This simulation treats the height of each single fibril as a stochastic property, which is modulated about the intended value. A randomly distributed error is used to offset the fibril height. This produces an array having fibrils with different height experiencing a different preload once the adhesive starts detaching from the adhered surface. The longer fibrils will experience a compressive preload, while the shorter fibrils will experience a tensile preload. This is done both for arrays having a uniform compliance distribution and for arrays having an optimized compliance distribution. The statistical variation of fibril length affects not only fibril preload but also fibril compliance. The same simulations are run multiple times generating arrays with increasing standard deviation in the stochastic variability of fibril height. Figure-26 shows the results of the Monte Carlo simulation and demonstrates that an optimized array outperforms an array with intended uniform compliance for a standard deviation that goes beyond 20%. The optimized arrays show a greater sensitivity to random deviation in height. The compliance optimization still provides a benefit in adhesive strength, compared with a homogeneous compliance distribution. For a standard deviation in fibril length that is around 20%, the benefit from compliance optimization in adhesive strength is around 5% for square arrays and around 10% for circular arrays.

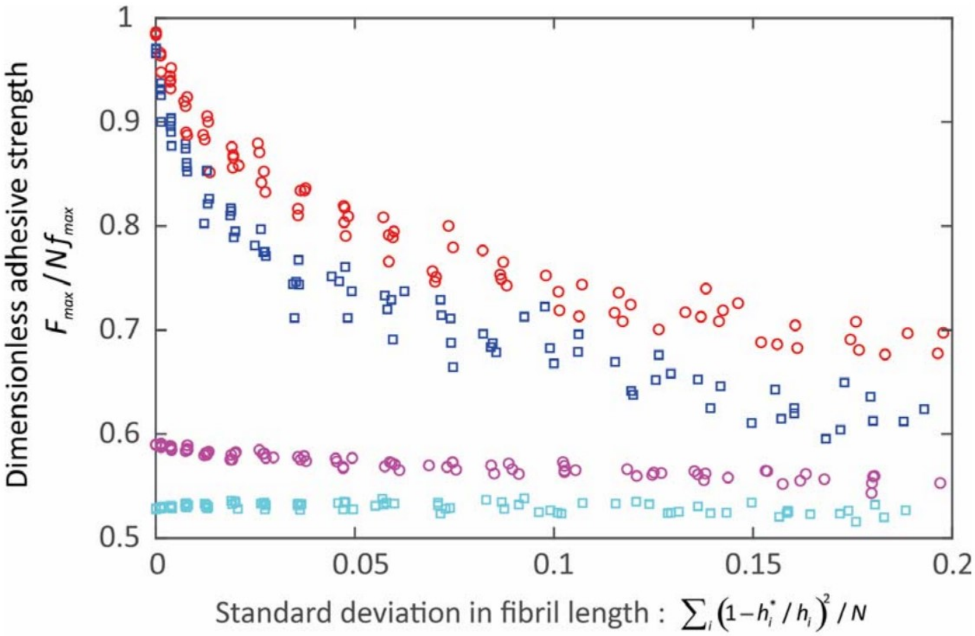

Figure 26: Dimensionless adhesive strength versus standard deviation in fibril length as the results of a Monte Carlo simulation. Blue squares indicate optimal compliance distribution for square arrays and cyan squares indicate square arrays with uniform distribution. Red circles indicate circular arrays with optimal compliance distribution, while purple circles indicate arrays with uniform compliance.

3.2.5 Discussion

The adhesive strength obtained from arrays optimized with the proposed asymptotic solution shows lower sensitivity to misalignment, compared with the ones optimized via numerical solution, and in some cases even higher value. The latter phenomenon is likely related to the significant stress redistribution generated by large misalignments, which challenges the benefits obtained from the optimal distribution of fibril compliance since the latter was constructed under the hypothesis of $\theta_d = 0$. The benefit emerged from the asymptotic approximation suggests the possibility of exploring array optimization for a range of misalignment angles instead of simply assuming a specific value for θ_d when calculating the optimal compliance distribution. This is beyond the scope of the current dissertation, hence is left for future work.

To achieve ELS at the array scale, functional grading of the fibril compliance distribution can potentially be done in multiple ways. For example, the Young modulus of the material composing the fibrils could be graded so that for fibril i, $^{E_{f,i}}/_{E_f} = {}^{c_m}/_{c_i^*}$ substituted in the numerical solution from [28], while for the continuum ensemble of fibrils, $^{E_f(x,y)}/_{E_f} = {}^{c_m}/_{c^*(x,y)}$ is substituted into Equation-45. Another way to achieve optimal compliance distribution is tailoring the length of each fibril following the relation $^{h_i}/_{h} = {}^{c_i^*}/_{c_m}$ or $^{h(x,y)}/_{h} = {}^{c^*(x,y)}/_{c_m}$. In this case, different fibril lengths within the same array would make it difficult for all the fibrils to adhere perfectly to the RS. This is because the longest fibrils will likely undergo buckling, and therefore, lose contact, in order to allow for the shortest ones to enter into contact. To counteract this effect, the RS or the BL should have a properly curved surface so that uniform contact across the interface can be achieved. The requirement for a specific curvature at the RS surface would significantly limit the applicability of the adhesive. The requirement of a properly curved BL surface, on the other hand, appears much less limiting; however, the proposed model should be modified to account for this feature. Finally, another method to achieve ELS is functional grading of the stalk radius of the fibrils, following $^{a_i}/_{a} = \sqrt{^{c_m}/_{c_i^*}}$ or $^{a(x,y)}/_{a} = \sqrt{^{c_m}/_{c^*(x,y)}}$.

An important design limitation related to functional grading of fibril compliance is the incremented risk of mutual adhesion among fibrils, also called fibril condensation [25], for the softest fibrils located at the perimeter of the contact region. This is because of the proportionality between axial stiffness and bending stiffness in a fibril, with bending stiffness being responsible for the prevention of fibril condensation. Since the closed-form solution presents the parameters that influence the stiffness gradient, one can infer that functional grading of the fibril modulus $E_{f,i}$ appears to be the most convenient strategy. This is because both axial stiffness and bending stiffness are linearly proportional to the fibril modulus. The other two methods instead appear to be suboptimal since bending stiffness decreases more rapidly than axial stiffness for an increment of stalk length h_i and a reduction of stalk radius a_i.

To mitigate the phenomenon of fibril condensation, one could reduce the contrast between maximum and minimum optimal compliance (in order to reduce the maximum compliance). Equation-45 evidences how this contrast is proportional to the term $\rho(^{E_f}/_{E^*})(^{R}/_{h})$, suggesting its minimization as a viable strategy. At this purpose, one could reduce the contrast in optimal compliance by reducing the fibril stalk density ρ. From Equation-41, one can deduce that this would imply a reduction in the fibril stalk radius, hence a reduction in bending stiffness, therefore requiring proper consideration. A significant reduction in stalk radius would also increment the stress experienced by the fibril at detachment, incrementing the risk of failure of the material composing the fibril. Another approach is the reduction of the ratio $^{E_f}/_{E^*}$ by producing softer fibrils or stiffer BL. The reduction in fibril modulus comes again at the price of a reduction in bending stiffness but less so than a reduction in ρ. A stiffer BL would give instead more effective results but only in the presence of negligible misalignment. This is because a softer BL has been observed to better resist interfacial misalignment ($\theta \neq 0$) [24, 28]. Finally, one can reduce the ratio $^{R}/_{h}$ by incrementing the overall fibril length h or by reducing the size of the array, via reduction of R. The former produces a significant loss in bending stiffness, as explained above, while the latter requires a reduction of the area of adhesive contact with the consequent reduction of the maximum detachment force. This limitation can be mitigated by the division of the contact region into multiple sub-regions with independent arrays of fibrils. Such a hierarchical fibrillar subdivision in multiple arrays is often observed in nature but its development in engineering prototypes brings again new challenges. Experimental validation of the proposed method requires the creation of an adhesive prototype having functionally graded fibril compliance. The stiffness of an elastomer can be controlled via crosslink density and inclusions. This process is feasible in principle; however, it is complicated and requires further development. An experimental proof of concept of our method, however, is proposed by Kumar et al. [31], where shear adhesion is improved by a graded compliance at the interface.

4 Conclusions and Future Work

4.1 Interfacial Curvature in Finite Thickness Arrays

We provide a quantitative analysis of the detachment kinetic and the adhesive strength of a fibrillar adhesive in the presence of interfacial curvature. While a (positive) curvature prompting higher stretch to peripheral fibrils always produces a reduction in strength, a (negative) curvature prompting higher stretch to central fibrils can produce an increment in strength. This effect emerges from the competition between BL interaction and curvature. The strength increment produced by curvature is therefore limited to relatively small curvatures, depending from the BL thickness. Higher BL thickness increments BL interaction, giving a larger margin for curvature-induced strengthening. Interfacial curvature can be prompted by a soft actuator on the BL or by forcing the fibrils to conform to a curved RS. In the former case, the actuation of curvature can also be used to prompt easy detachment (with positive curvature) for an enhanced adhesion control. The ability of the curvature to improve the arrays strength upholds even in the presence of misalignment. In fact, the sensitivity to misalignment decreases with the implementation of negative curvature.

4.2 Asymptotic Approximation

The accuracy of our asymptotic model, in generating ELS for zero misalignment, increases with the density of the array. We performed multiple numerical simulations with various N and ρ for both circular and square arrays utilizing the asymptotic solution for optimal compliance distribution, from Equation-48 and 52, respectively. For the circular arrays, the number of fibrils were varied from 208 to 1804 for a constant radius of $R/a = 80$. This varied the fibrillar density from 0.1 to 0.3 and resulted in a minimum load sharing efficiency of 0.98. For the square array, the number of fibrils was varied from 289 to 2401 for a constant radius of $R/a = 80$. This also varied the fibrillar density from 0.1 to 0.3, and again resulted in a minimum load sharing efficiency of 0.98. In conclusion, for both circular and square arrays, the results indicated a deviation in adhesive strength that is within 2%, compared with ELS. All this for $\theta_d = 0$ and $\theta = 0$ for square arrays and circular arrays, taken as representative cases for a wide range of practical applications. For the case of $\theta \neq 0$, the asymptotic approximation demonstrated some benefits in terms of reduced sensitivity of strength versus misalignment and even higher strength, for $|\theta| > |\theta_{tr}|$.

The proposed asymptotic analysis provides the numerous benefits of a closed-form solution, evidencing the determinants of an optimal interfacial stiffness distribution to reduce stress concentration, and hence achieve ELS, at the fibril array level. We demonstrated the robustness of the proposed compliance optimization algorithm in providing higher adhesive strength also in the presence of statistical imperfections in fibrils' length. Our model system can be further generalized beyond fibrillar adhesives if used in an analogy that considers fibrils as brittle bonds uniformly distributed across an interface separated by a tensile load. Our solution indeed suggests a theoretical strategy to achieve maximum toughness of an adhesive interface by grading the stiffness of its bonds. Incremented strength in adhesive interfaces designed with proper compliance grading has been experimentally observed in shear adhesion [31]. Although shear adhesion is a different phenomenon than that analyzed in this paper, both adhesion mechanisms are controlled by stress concentration; hence, the aforementioned experimental findings are to be taken as a qualitative validation of our theory.

4.3 Future Works

The most pressing future work is an experimental validation of the finite thickness BL correction factors. The results generated by the model will be compared with the results of [24], to validate whether the sensitivity to misalignment can be quantitatively predicted. Another experimental validation of the model will be attempted with array aspect ratios and how that effects the sensitivity to misalignment. The experimental procedure for this has been outline in Appendix A.

A third future work involves expanding the displacement input model for viscoelastic materials instead of just linear elastic. An attempted method involved treating the fibrils as behaving with linear viscoelasticity while the BL was still entirely linear elastic. This assumed that BL displacements were small relative to the fibrillar elongation which could not be validated with the results of the simulation. This project requires investigation into the displacement profile of a viscoelastic BL in response to a concentrated force.

Bibliography

[1] *Attachment Devices of Insect Cuticle*. Kluwer Academic Publishers, 2002. DOI: 10.1007/0-306-47515-4. URL: https://doi.org/10.1007/0-306-47515-4.

[2] Kellar Autumn. "Properties, Principles, and Parameters of the Gecko Adhesive System". In: *Biological Adhesives*. Ed. by Andrew M. Smith and James A. Callow. Berlin, Heidelberg: Springer Berlin Heidelberg, 2006, pp. 225–256. ISBN: 978-3-540-31049-5. DOI: 10.1007/978-3-540-31049-5_12. URL: https://doi.org/10.1007/978-3-540-31049-5_12.

[3] Stanislav N. Gorb and Michael Varenberg. "Mushroom-shaped geometry of contact elements in biological adhesive systems". In: *Journal of Adhesion Science and Technology* 21.12-13 (2007), pp. 1175–1183. DOI: 10.1163/156856107782328317. eprint: https://doi.org/10.1163/156856107782328317. URL: https://doi.org/10.1163/156856107782328317.

[4] Haimin Yao and Huajian Gao. "Mechanics of robust and releasable adhesion in biology: Bottom–up designed hierarchical structures of gecko". In: *Journal of the Mechanics and Physics of Solids* 54.6 (2006), pp. 1120–1146. ISSN: 0022-5096. DOI: https://doi.org/10.1016/j.jmps.2006.01.002. URL: http://www.sciencedirect.com/science/article/pii/S0022509606000056.

[5] Kellar Autumn et al. "Adhesive force of a single gecko foot-hair". English. In: *Nature* 405.6787 (June 2000). Copyright - Copyright Macmillan Journals Ltd. Jun 8, 2000; Last updated - 2019-09-06; CODEN - NATUAS, pp. 681–5. URL: http://ezproxy.library.ubc.ca/login?url=https://search-proquest-com.ezproxy.library.ubc.ca/docview/204486957?accountid=14656.

[6] Kellar Autumn and Anne M. Peattie. "Mechanisms of Adhesion in Geckos". In: *Integrative and Comparative Biology* 42.6 (2002), pp. 1081–1090. ISSN: 15407063, 15577023. URL: http://www.jstor.org/stable/3884747.

[7] K. Autumn et al. "Evidence for van der Waals adhesion in gecko setae". In: *Proceedings of the National Academy of Sciences* 99.19 (Aug. 2002), pp. 12252–12256. DOI: 10.1073/pnas.192252799. URL: https://doi.org/10.1073/pnas.192252799.

[8] G. J. Lake and A. G. Thomas. "The Strength of Highly Elastic Materials". In: *Proceedings of the Royal Society of London. Series A, Mathematical and Physical Sciences* 300.1460 (1967), pp. 108–119. ISSN: 00804630. URL: http://www.jstor.org/stable/2415748.

[9] Todd M. Mower and Ali S. Argon. "Experimental investigations of crack trapping in brittle heterogeneous solids". In: *Mechanics of Materials* 19.4 (1995), pp. 343–364. ISSN: 0167-6636. DOI: https://doi.org/10.1016/0167-6636(94)00042-F. URL: http://www.sciencedirect.com/science/article/pii/016766369400042F.

[10] B. N. J. Persson and S. Gorb. "The effect of surface roughness on the adhesion of elastic plates with application to biological systems". In: *The Journal of Chemical Physics* 119.21 (2003), pp. 11437–11444. DOI: 10.1063/1.1621854. eprint: https://doi.org/10.1063/1.1621854. URL: https://doi.org/10.1063/1.1621854.

[11] N. J. Glassmaker et al. "Design of biomimetic fibrillar interfaces: 1. Making contact". In: *Journal of The Royal Society Interface* 1.1 (Nov. 2004), pp. 23–33. DOI: 10.1098/rsif.2004.0004. URL: https://doi.org/10.1098/rsif.2004.0004.

[12] K. Autumn et al. "Effective elastic modulus of isolated gecko setal arrays". In: *Journal of Experimental Biology* 209.18 (2006), pp. 3558–3568. ISSN: 0022-0949. DOI: 10.1242/jeb.02469. eprint: https://jeb.biologists.org/content/209/18/3558.full.pdf. URL: https://jeb.biologists.org/content/209/18/3558.

[13] Tae Wan Kim and Bharat Bhushan. "Effect of stiffness of multi-level hierarchical attachment system on adhesion enhancement". In: *Ultramicroscopy* 107.10-11 (Oct. 2007), pp. 902–912. ISSN: 0304-3991. DOI: 10.1016/j.ultramic.2006.11.008. URL: https://doi.org/10.1016/j.ultramic.2006.11.008.

[14] Eduard Arzt, Stanislav Gorb, and Ralph Spolenak. "From micro to nano contacts in biological attachment devices". In: *Proceedings of the National Academy of Sciences* 100.19 (2003), pp. 10603–10606. ISSN: 0027-8424. DOI: 10.1073/pnas.1534701100. eprint: https://www.pnas.org/content/100/19/10603.full.pdf. URL: https://www.pnas.org/content/100/19/10603.

[15] H. Gao and H. Yao. "Shape insensitive optimal adhesion of nanoscale fibrillar structures". In: *Proceedings of the National Academy of Sciences* 101.21 (May 2004), pp. 7851–7856. DOI: 10.1073/pnas.0400757101. URL: https://doi.org/10.1073/pnas.0400757101.

[16] Huajian Gao et al. "Mechanics of hierarchical adhesion structures of geckos". In: *Mechanics of Materials* 37.2 (2005). New Directions in Mechanics and Selected Articles in Micromechanics of Materials, pp. 275–285. ISSN: 0167-6636. DOI: https://doi.org/10.1016/j.mechmat.2004.03.008. URL: http://www.sciencedirect.com/science/article/pii/S0167663604000833.

[17] Robert M. McMeeking, Eduard Arzt, and Anthony G. Evans. "Defect Dependent Adhesion of Fibrillar Surfaces". In: *The Journal of Adhesion* 84.7 (2008), pp. 675–681. DOI: 10.1080/00218460802255558. eprint: https://doi.org/10.1080/00218460802255558. URL: https://doi.org/10.1080/00218460802255558.

[18] Jamie A. Booth et al. "Statistical properties of defect-dependent detachment strength in bioinspired dry adhesives". In: *Journal of The Royal Society Interface* 16.156 (July 2019), p. 20190239. DOI: 10.1098/rsif.2019.0239. URL: https://doi.org/10.1098/rsif.2019.0239.

[19] A. del Campo et al. "Patterned Surfaces with Pillars with Controlled 3D Tip Geometry Mimicking Bioattachment Devices". In: *Advanced Materials* 19.15 (Aug. 2007), pp. 1973–1977. DOI: 10.1002/adma.200602476. URL: https://doi.org/10.1002/adma.200602476.

[20] Aránzazu del Campo, Christian Greiner, and Eduard Arzt. "Contact Shape Controls Adhesion of Bioinspired Fibrillar Surfaces". In: *Langmuir* 23.20 (2007). PMID: 17722937, pp. 10235–10243. DOI: 10.1021/la7010502. eprint: https://doi.org/10.1021/la7010502. URL: https://doi.org/10.1021/la7010502.

[21] Seok Kim and Metin Sitti. "Biologically inspired polymer microfibers with spatulate tips as repeatable fibrillar adhesives". In: *Applied Physics Letters* 89.26 (2006), p. 261911. DOI: 10.1063/1.2424442. eprint: https://doi.org/10.1063/1.2424442. URL: https://doi.org/10.1063/1.2424442.

[22] Henrik Peisker, Jan Michels, and Stanislav N. Gorb. "Evidence for a material gradient in the adhesive tarsal setae of the ladybird beetle Coccinella septempunctata". In: *Nature Communications* 4.1 (Apr. 2013). DOI: 10.1038/ncomms2576. URL: https://doi.org/10.1038/ncomms2576.

[23] Stanislav N. Gorb and Alexander E. Filippov. In: *Beilstein Journal of Nanotechnology* 5 (2014), pp. 837–845. DOI: 10.3762/bjnano.5.95.

[24] Jamie A. Booth et al. "Benefit of Backing-Layer Compliance in Fibrillar Adhesive Patches—Resistance to Peel Propagation in the Presence of Interfacial Misalignment". In: *Advanced Materials Interfaces* 5.15 (2018), p. 1800272. DOI: 10.1002/admi.201800272. eprint: https://onlinelibrary.wiley.com/doi/pdf/10.1002/admi.201800272. URL: https://onlinelibrary.wiley.com/doi/abs/10.1002/admi.201800272.

[25] Ralph Spolenak, Stanislav Gorb, and Eduard Arzt. "Adhesion design maps for bio-inspired attachment systems". In: *Acta Biomaterialia* 1.1 (2005), pp. 5–13. ISSN: 1742-7061. DOI: https://doi.org/10.1016/j.actbio.2004.08.004. URL: http://www.sciencedirect.com/science/article/pii/S1742706104000030.

[26] Haimin Yao and Huajian Gao. "Gibson-Soil-Like Materials Achieve Flaw-Tolerant Adhesion". In: *Journal of Computational and Theoretical Nanoscience* 7.7 (2010), pp. 1299–1305. ISSN: 1546-1955. DOI: doi:10.1166/jctn.2010.1484. URL: https://www.ingentaconnect.com/content/asp/jctn/2010/00000007/00000007/art00012.

[27] Yang Gao and Haimin Yao. "Homogenizing interfacial shear stress via thickness gradient". In: *Journal of the Mechanics and Physics of Solids* 131 (2019), pp. 112–124. ISSN: 0022-5096. DOI: https://doi.org/10.1016/j.jmps.2019.06.017. URL: http://www.sciencedirect.com/science/article/pii/S0022509619303539.

[28] Mattia Bacca et al. "Load sharing in bioinspired fibrillar adhesives with backing layer interactions and interfacial misalignment". In: *Journal of the Mechanics and Physics of Solids* 96 (2016), pp. 428–444. ISSN: 0022-5096. DOI: https://doi.org/10.1016/j.jmps.2016.04.008. URL: http://www.sciencedirect.com/science/article/pii/S0022509616301508.

[29] Rong Long et al. "Modeling the soft backing layer thickness effect on adhesion of elastic microfiber arrays". In: *Journal of Applied Physics* 104.4 (2008), p. 044301. DOI: 10.1063/1.2968249. eprint: https://doi.org/10.1063/1.2968249. URL: https://doi.org/10.1063/1.2968249.

[30] Harman Khungura and Mattia Bacca. "Optimal load sharing in bioinspired fibrillar adhesives: Asymptotic solution". In: *Journal of Applied Mechanics* (July 2020), pp. 1–15. ISSN: 0021-8936. DOI: 10.1115/1.4047859. eprint: https://asmedigitalcollection.asme.org/appliedmechanics/article-pdf/doi/10.1115/1.4047859/6551377/jam-20-1325.pdf. URL: https://doi.org/10.1115/1.4047859.

[31] Shanmugam Kumar et al. "Stress Reduction of 3D Printed Compliance-Tailored Multilayers". In: *Advanced Engineering Materials* 20.1 (2018), p. 1700883. DOI: 10.1002/adem.201700883. eprint: https://onlinelibrary.wiley.com/doi/pdf/10.1002/adem.201700883. URL: https://onlinelibrary.wiley.com/doi/abs/10.1002/adem.201700883.

[32] G.M. Guidoni et al. "Discrete contact mechanics of a fibrillar surface with backing layer interactions". In: *Journal of the Mechanics and Physics of Solids* 58.10 (2010), pp. 1571–1581. ISSN: 0022-5096. DOI: https://doi.org/10.1016/j.jmps.2010.07.009. URL: http://www.sciencedirect.com/science/article/pii/S0022509610001389.

[33] W. L. Noderer et al. "Enhanced Adhesion and Compliance of Film-Terminated Fibrillar Surfaces". In: *Proceedings: Mathematical, Physical and Engineering Sciences* 463.2086 (2007), pp. 2631–2654. ISSN: 13645021. URL: http://www.jstor.org/stable/20209335.

[34] K.L. Johnson. Cambridge University Press, 1985. ISBN: 978-0-521-34796-9. URL: https://app.knovel.com/hotlink/toc/id:kpCM000008/contact-mechanics/contact-mechanics.

[35] M. Schargott, V.L. Popov, and S. Gorb. "Spring model of biological attachment pads". In: *Journal of Theoretical Biology* 243.1 (2006), pp. 48–53. ISSN: 0022-5193. DOI: https://doi.org/10.1016/j.jtbi.2006.05.023. URL: http://www.sciencedirect.com/science/article/pii/S0022519306001986.

[36] Julie Diani, Bruno Fayolle, and Pierre Gilormini. "A review on the Mullins effect". In: *European Polymer Journal* 45.3 (2009), pp. 601–612. ISSN: 0014-3057. DOI: https://doi.org/10.1016/j.eurpolymj.2008.11.017. URL: http://www.sciencedirect.com/science/article/pii/S0014305708006332.

Appendices

Appendix A: Experimental Setup

The experimental work was performed at the Leibniz Institute for New Materials at the University of Saarland. Testing the adhesive samples was done on a Hegewald & Peschke Inspekt Table Blue Universal Testing Machine. The tensile testing machine operates within a close able chamber that limits free flowing air and external light. Additionally the position and motion of the tester's arm is controlled via software from a desktop computer.

The adhesive samples were prepared from a thermoplastic polyurethane. The tip geometry of the adhesive fibrils was of a mushroom tip design and the fibrils themselves were arranged in a hexagonal pattern. Measurements on the adhesive's physical parameters were made using a Keyence digital light microscope. The microscope was focused into specific zones of the adhesive to measure parameters of fibrillar geometry as shown in Figure-27a and Figure-27b. The measurements for each respective zone was recorded and then averaged to be taken as a constant throughout the array. After measurements, the adhesive sample was lightly washed in acetone to remove the build up of dust and various air debris on the fibril tips. A double sided tape was applied to the backing layer of the adhesive sample to couple it with the tensile tester.

Glass substrates of varying aspect ratio were made from microscope slides. The microscope slides were marked and cut by hand using a glass cutter. Once cut, the edges of the substrates were sanded with 1000-1200 grit sandpaper to prevent sharp edges from cutting or damaging the fibril tips that would come into contact with them at the perimeter. Once the edges were smoothed, the substrates were submerged into ispropanol and placed into an ultrasonic bath to remove any oils on their surface. Once cleaned, the substrates were adhered to a larger glass substrate using PDMS and cured in an oven for 1 hour. The experimental setup is labelled in Figure-28.

The principle of frustrated total internal reflection was utilized to capture video of adhesion tests. Light was shined into the glass substrates along their circumference. Then, as the fibril tips came into contact with the glass substrate, light rays scatter and reflect into the camera as shown in Figure-29a. Video for each tensile test was capture using a DMK33GX236, Imaging Source Europe GmbH, Bremen, Germany. A picture of this setup is also shown in Figure-29b.

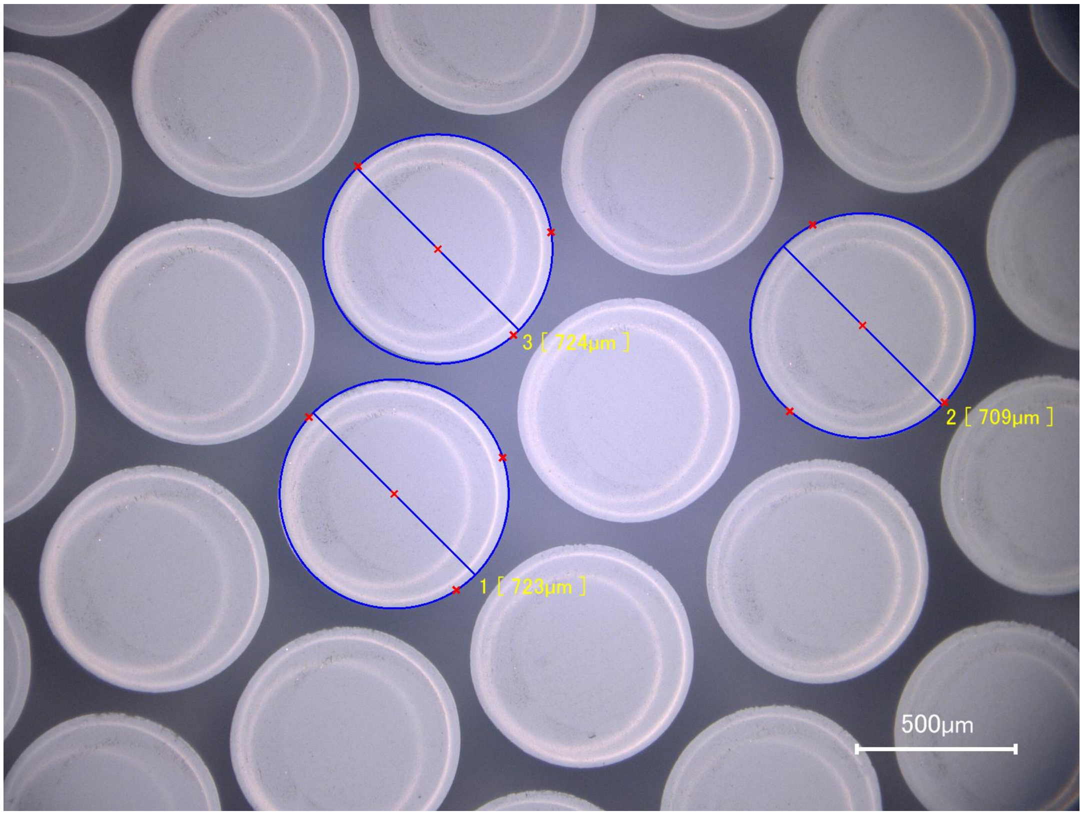

(a) Top down view of a fibrillar adhesive sample.

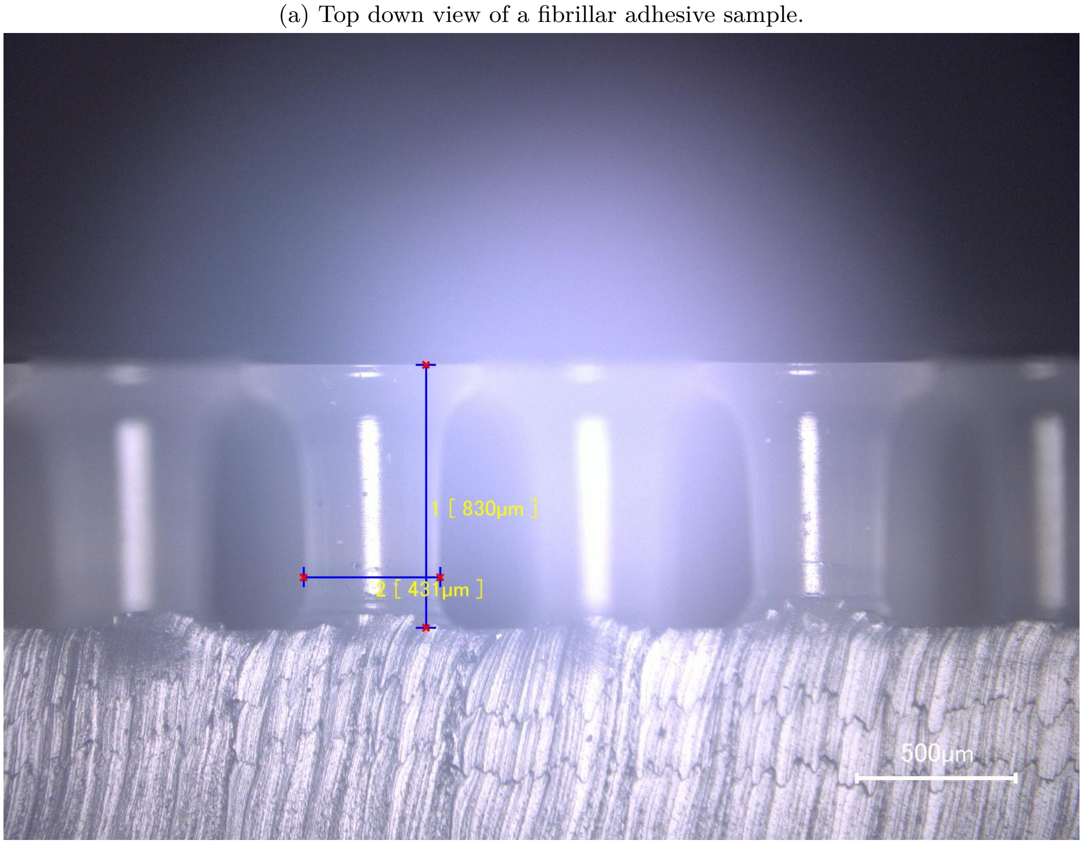

(b) Front facing view of a fibrillar adhesive sample.

Figure 27: Close up images of fibrils and pillars of an adhesive sample under the Keyence light microscope.

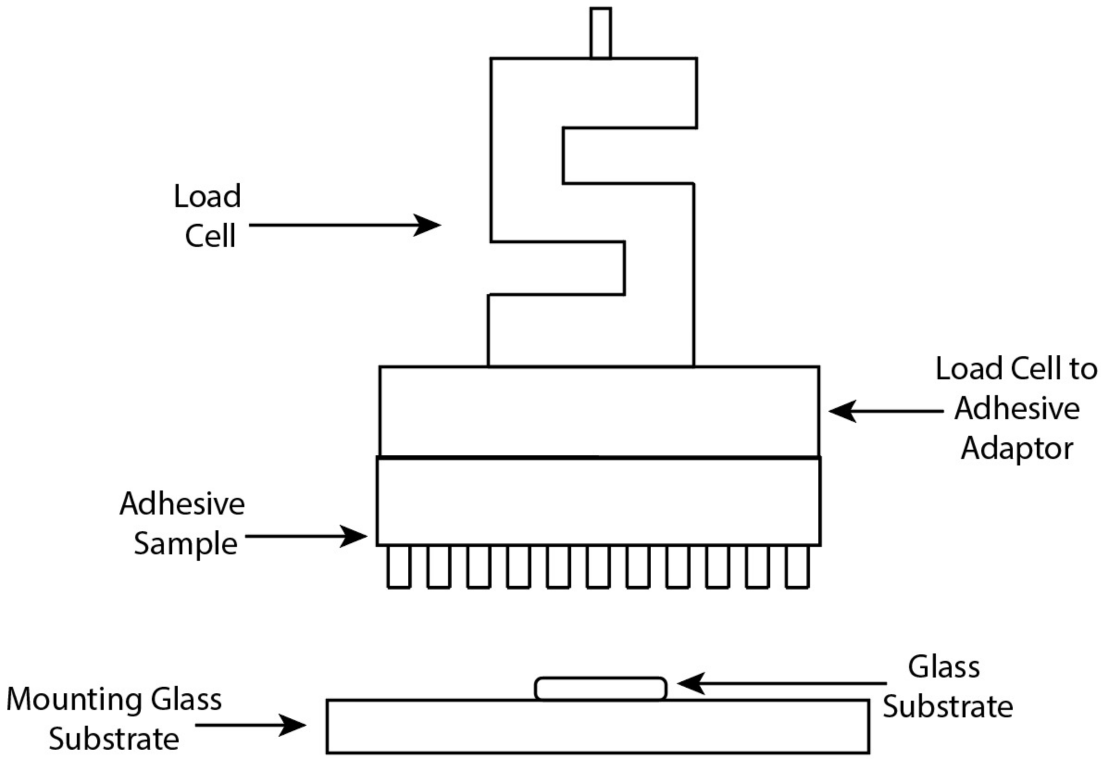

Figure 28: Labelled diagram for the testing setup of tensile tests in the Hegewald & Peschke Inspekt Table Blue Universal Testing Machine.

The testing of the samples was done in a normalized manner to minimize variations and alterations in conditions of properties of anything involved. The adhesive sample was brought into contact with the glass substrate at $1\frac{mm}{min}$ until all fibrils came into contact and were sufficiently pre-loaded. The local detachment force of a fibril increases with the compressive pre-load that is applied to it, until it enters a saturation zone and eventually buckles as illustrated in Figure-30.

Once a fibril has approached the saturation zone, variations in pre-load do not significantly affect the adhesive strength of that fibril. This is greatly beneficial for testing arrays with misalignment at the adhesive interface, as the local detachment force can be assumed constant throughout the array. It should be noted that during the pre-loading step, fibrils along the direction of the misalignment will not simultaneously make contact with the rigid substrate. This is seen in Figure-31a, where fibrils make first contact with the bottom of the substrate resulting in a greater compressive pre-load. This also results in the fibrils at the bottom being more susceptible to buckling as shown in Figure-31b.

Once all fibrils were saturated with pre-load, the substrate was held in contact for $1s$ and retracted at

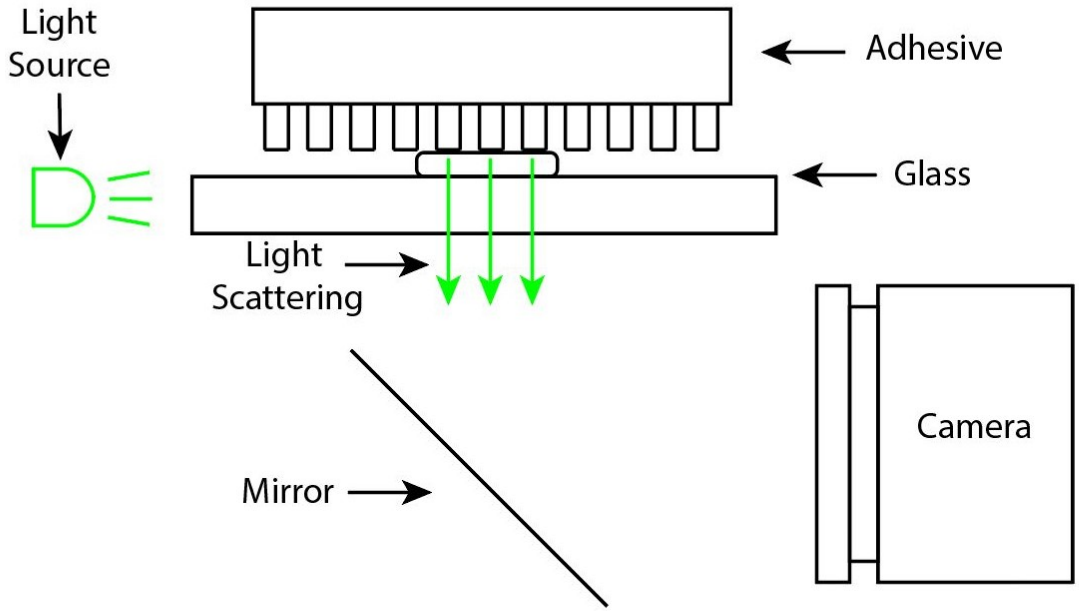

(a) Diagram of how frustrated total internal reflection was utilized to capture video for the adhesion tests.

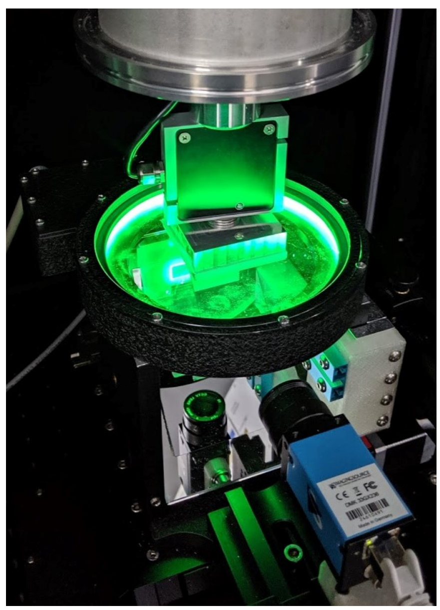

(b) A picture of the adhesive test setup. Green light is shined into the glass substrates and reflects off a mirror into the camera.

Figure 29: A schematic diagram and image illustrating the working principle behind the frustrated total internal reflection principle.

$10\frac{mm}{min}$. Throughout the test, the force displacement graph and maximum force is recorded. Testing trials were held between three minute intervals to ensure that the frequency of loading on the polyurethane remained constant (cite frequency of loading). During these three minute intervals, the adhering side of scotch tape was applied to the ends of the fibril tips and then removed to remove any build up of dust or debris on the fibril tips. Furthermore, acetone was applied to a

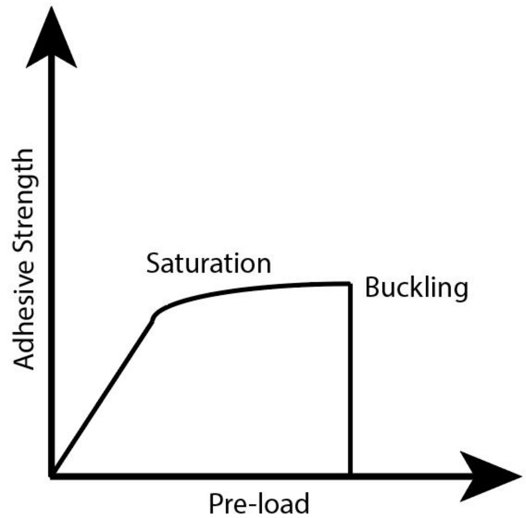

Figure 30: A qualitative plot of the adhesive strength vs. pre-loading performed on a fibril prior to tensile testing.

cotton cloth and used to wipe the glass substrate to clean its surface as well of any accumulating dust or debris.

The local detachment force for each fibril was approximated by imposing a large misalignment on a test with a large aspect ratio. This results in only a perimeter strip of several fibrils adhering to the substrate. The adhesive was then retracted from the substrate and the ultimate force recorded was assumed to occur with equal load sharing amongst the number of fibrils in contact. The assumption of equal load sharing is based on the principle that load sharing efficiency of an array approaches 100% as the number of fibrils in contact decreases [28].

The computational model explained in Section-2.1.1 had to be modified for a hexagonal distribution of fibrils and the mushroom tipped fibril geometry. In addition, correction factors are required to account for the softening of the polyurethane adhesive sample after multiple tests [36]. The correctional factors from Section-2.1.3 will also need to be used as the BL thickness is not large compared to the fibril length scales.

The computational model for fibrillar detachment assumes that detachment occurs when the local forces results in a stress corresponding to a critical axial strain. In other words, it will be assumed that contact between the fibril tip and the displacing rigid surface is perfect, meaning that no centre or edge crack propagation is the driving force behind detachment. Instead, the fibril force will be computed with the stalk radius of the fibril as in done in the expression:

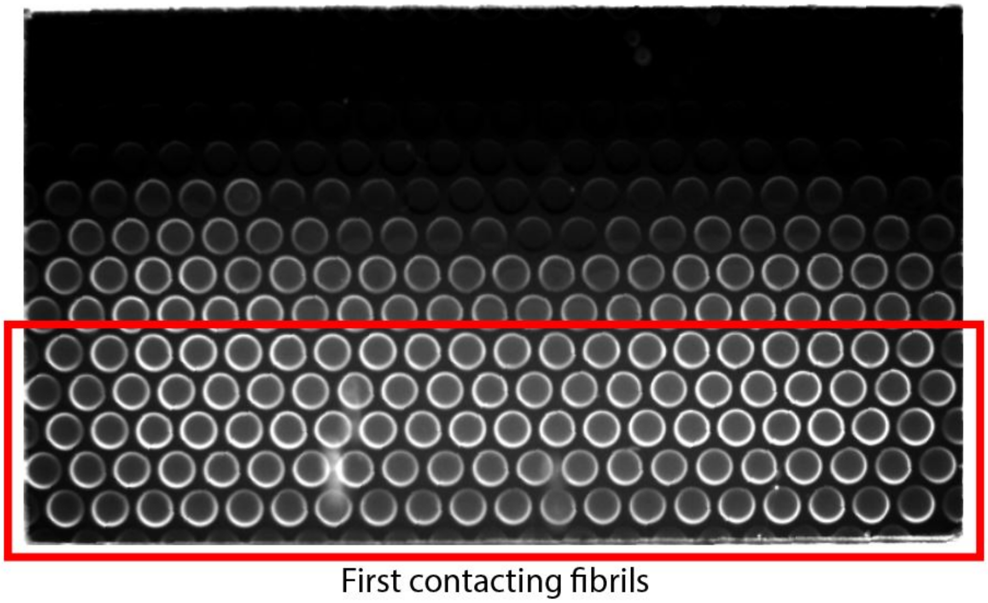

(a) A screenshot of the pre-loading stage during a test with misalignment at the interface. Fibrils at the bottom make first contact with the rigid substrate.

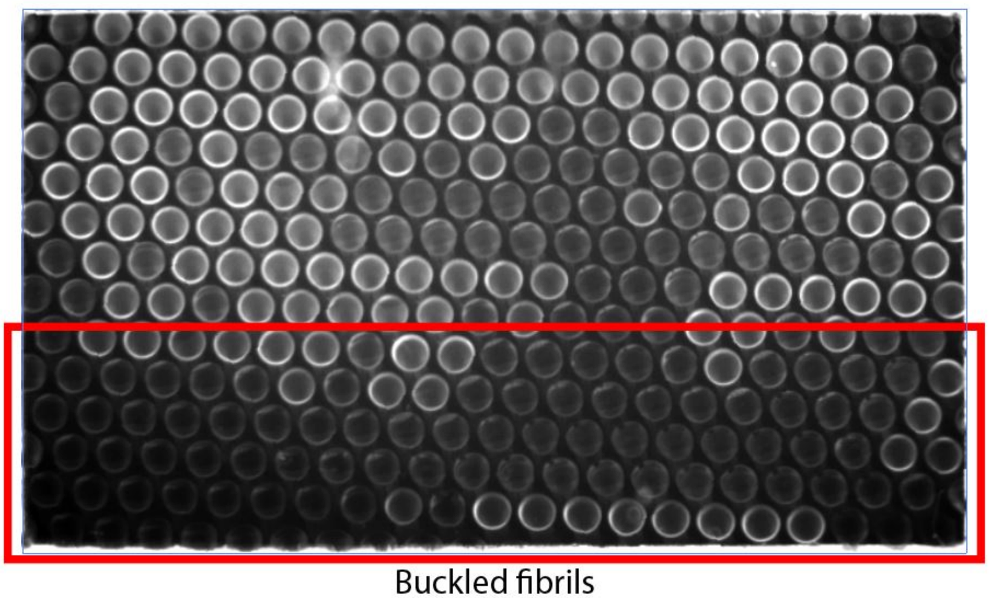

(b) A screenshot of the pre-loading stage where fibril buckling occurred. Fibrils at the bottom of the image buckled first.

$$C_{ij} = \frac{1}{\pi a_{stalk} E^*} \left[\frac{16}{3\pi} + \frac{h}{a_{stalk}(1-\nu^2)} \right], \quad \text{for } j = i \tag{53}$$

which revises Equation-9b. The same will occur for computing the limit for maximum misalignment which revises Equation-54 below.

$$\tan \theta^*_{xz} = \frac{h f_{max}}{\pi a^2_{stalk} E (n_x - 1) d} \tag{54}$$

A.1 Definition of Aspect Ratio

The aspect ratio of the arrays tested is defined be the contacting distance along the misalignment over the contacting distance orthogonal to the misalignment, as expressed in Equation-55 below.

$$\gamma = \frac{L_\theta}{L_\perp} \tag{55}$$

With the use of the multi-axis goniometer, the aspect ratio was inversed by switching the axis of rotation. The first benefit of this was maintaining a constant area of contact since the same adhering substrate was used. The second benefit of this was not adjust the reference aligned position of the pull tester and needed to re-align the experimental setup. This is exemplified in Figure-32a and Figure-32b, where the aspect ratio is switched from 2.86 to 0.35 solely through the orientation of misalignment. The benefit of this method is that the same adhering substrate can be used for 2 different aspect ratio and that the contact area does not change between tests.

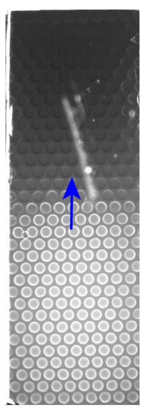

(a) The misalignment is oriented along the vertical axis. This creates an aspect ratio of $\gamma = 2.86$

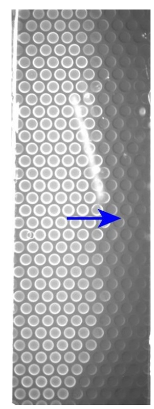

(b) The misalignment is oriented along the horizontal axis. This creates an aspect ratio of $\gamma = 0.35$

Figure 32: Screenshots of the a substrate being pre-loading for two different orientations of misalignment.

Due to the hexagonal distribution of the fibrils, the glass substrates did not perfectly align with the circumference of fibril tips. This results in partial contact between these fibrils and the adhering surface which inevitably leads to these fibrils having a reduced localized detachment force. It was observed that these partially contacting fibrils were the first ones to detach, and increased the stiffness of the system while adhered as in shown in Figure-33. Since these fibrils detach prior to the ultimate adhesive force being reached, they can be neglected and treated as inactive fibrils. It should be noted that Figure-33 also confirms the theoretical expectation of rapid detachment following the peak force.

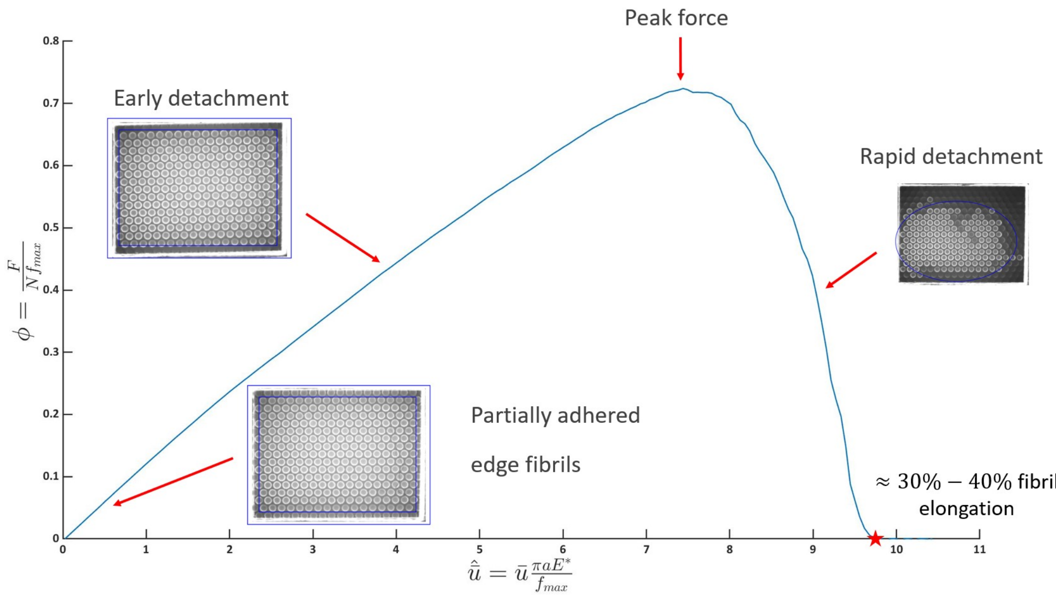

Figure 33: Force displacement curve recorded for the experimental trial of $\gamma = 2.86$ with $\theta = 0°$. The partially adhered fibrils increase the stiffness of the system until they detach.

Appendix B: Validating the Superposition of a Concentrated Normal Force on a Curved Backing Layer

To model the force displacement relationship of a fibril protruding from a curved backing layer, a finite element simulation was performed using two simplifications. The first was if the characteristic length of the backing layer is large compared to the thickness, it can be considered as an Euler-Bernoulli beam in pure bending. The second was if the radius of a fibril is small relative to both the thickness and characteristic length of the backing layer, than the fibrillar force can be considered a concentrated normal force. The latter has already been proven in [28].

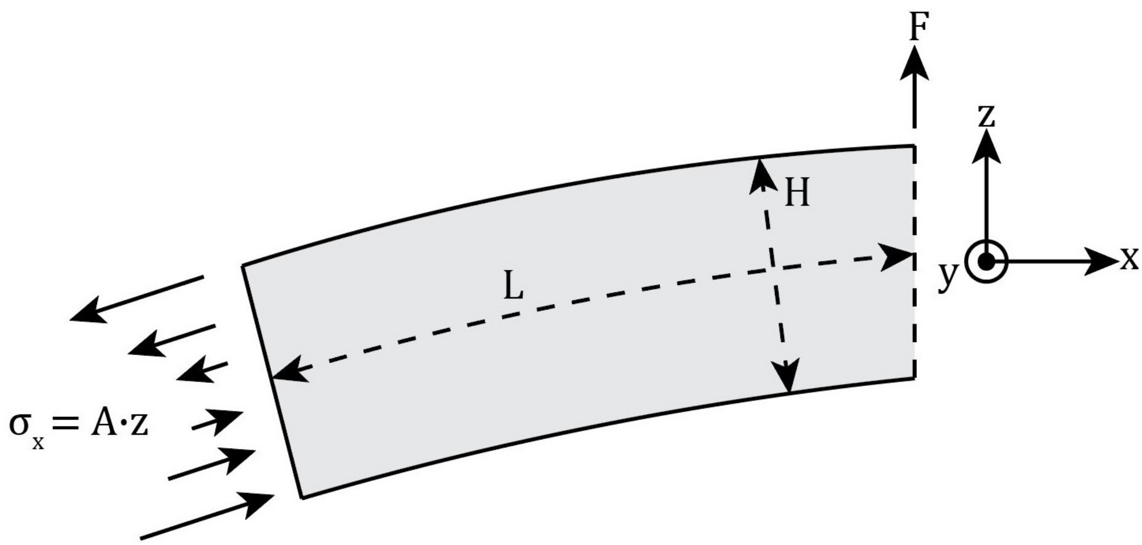

Figure 34: The FEA model used for the superposition of a concentrated normal force applied to a beam in bending.

The finite element model used to verify the superposition of concentrated force applied to a beam in bending is shown above in Figure-34. The beam has a characteristic length and width of $2L = 80$ and a thickness of $H = 20$ that is being bent by a varying normal stress $\sigma_x = Az$. The concentrated normal force is approximated by a uniform stress applied over a circular region, using the relationship $F = \sigma_z \pi a^2$ where a is the radius of a fibrillar unit.

The total moment acting on the backing layer is $M = AI$, where I is the area moment of inertia of the beams cross section. By treating the backing layer as an Euler-Bernoulli beam, the displacement profile due to this bending moment is

$$u_{BL,i} = -\frac{\kappa_x x_i^2}{2} + C_2 \tag{56}$$

where $\kappa_x = {}^{M}/_{EI}$ and C_2 is an integration constant that depends on the coordinate system. The displacements that would result from a concentrated normal force are given by the contact mechanics solution found in [34].

$$u_{BL,i} = \frac{\sigma_j a^2}{r_{ij} E^*} \tag{57}$$

where σ_j is the uniform stress applied by fibril j and r_{ij} is the centre to centre distance between fibrils i and j. To officially validate the superposition of the combined loading, the sum of Equation-56 and Equation-57 was compared to the FEA results as shown in Figure-35. All displacements are taken along the x-axis where $r_i = x_i$ and scaled by a factor of ${}^{E^*}/_{a\sigma^*}$ where σ^* is an arbitrary stress. Additionally, the coordinates are represented relative to fibril radius which give $\tilde{x} = {}^{x}/_{a}$.

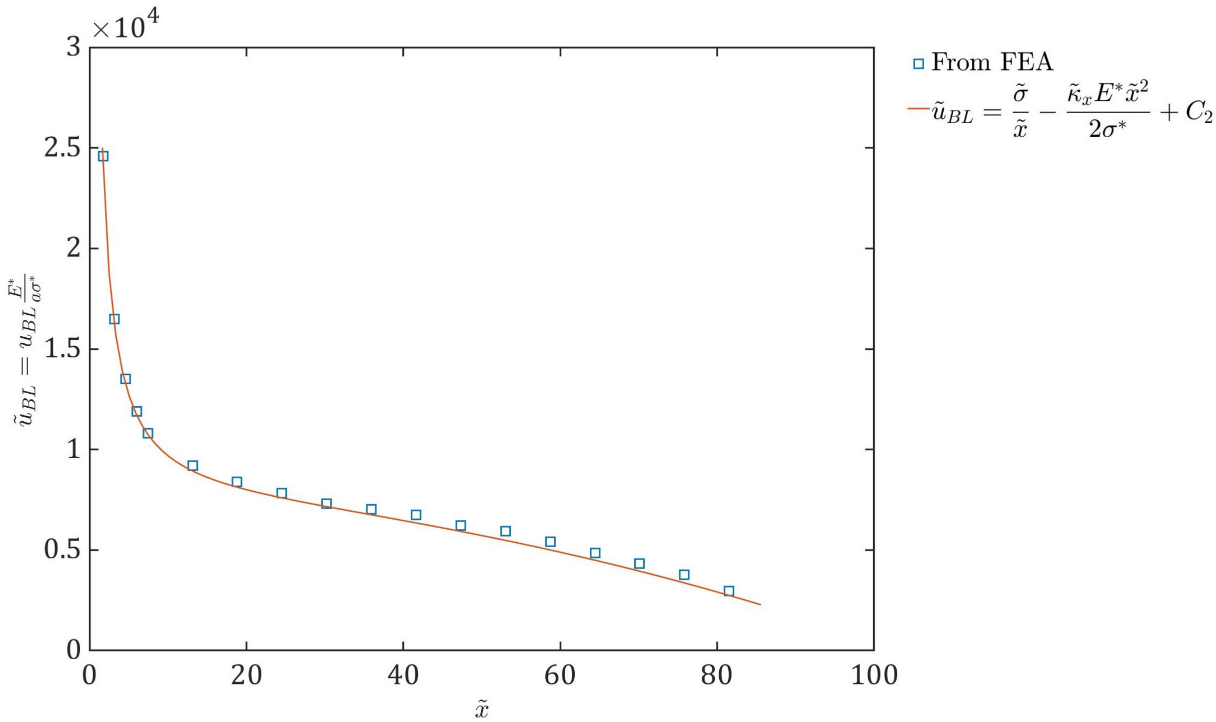

Figure 35: Comparing the FEA results of the combined loading case with the superposition of a concentrated normal force and Euler-Bernoulli beam in pure bending. $\hat{\sigma} = {}^{\sigma}/_{\sigma^*}$ and $\tilde{\kappa}_x = \kappa_x a$.

The curvature of the beam is given by $\chi_{BL} = {}^{|u''_{BL}|}/_{[1+(u'_{BL})^2]^{1.5}}$. Since only small moments will be applied to the model, it can be taken that $(u'_{BL})^2 \ll 1$ so the curvature of the beam can be defined as $\chi_{BL} = |u''_{BL}| = \chi_x$. For the purpose of this work, a backing layer that is curved upwards from its centre will be defined as having positive curvature or being concave up. Consequently, a backing layer that is curved downward from its centre will be defined as having negative curvature or being concave down. A concave up and concave down backing layer are shown in Figure-36a and Figure-36b respectively.

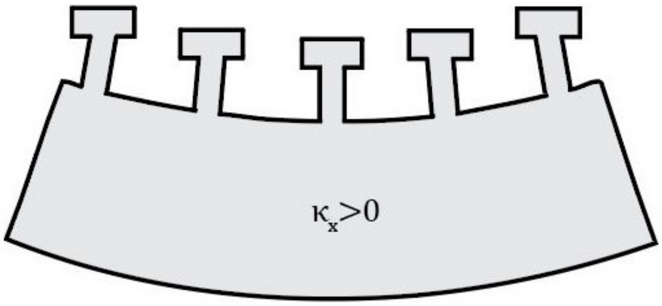

(a) A backing layer with upward concavity or positive curvature

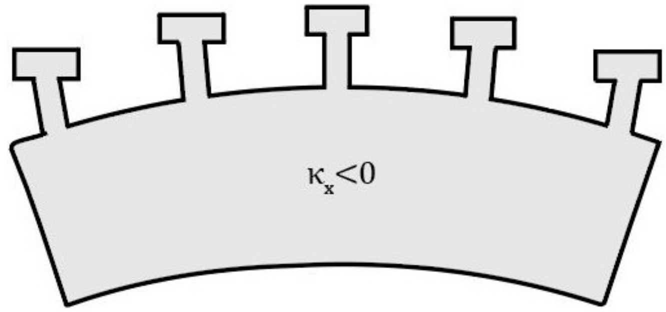

(b) A backing layer with downward concavity or negative curvature

Figure 36: Showcasing the definitions of backing layer curvature.